

Qualitative dynamics of wave packets in turbulent jets

Onofrio Semeraro,^{1,2,*} François Lusseyran,³ Luc Pastur,⁴ and Peter Jordan⁵

¹*DMMM, Politecnico di Bari, Bari, Italy*

²*LadHyX, CNRS, École polytechnique, Palaiseau, France*

³*LIMSI, CNRS, Université Paris-Saclay, Orsay, France*

⁴*LIMSI, CNRS, Université Paris-Sud, Université Paris-Saclay, Orsay, France*

⁵*Institut PPRIME, CNRS, Université de Poitiers, ENSMA, Poitiers, France*

(Received 25 August 2016; published 20 September 2017)

We analyze the temporal dynamics associated with axisymmetric coherent structures in a turbulent jet. It has long been established that turbulent jets comprise large-scale coherent structures, now more commonly referred to as “wave packets” [Jordan and Colonius, *Annu. Rev. Fluid Mech.* **45**, 173 (2013)]. These structures exhibit a marked spatiotemporal organization, despite turbulence, and we aim to characterize their temporal dynamics by means of nonlinear statistical tools. The analysis is based on data presented Breakey *et al.*, in *Proceedings of the 19th AIAA/CEAS Aeroacoustics Conference*, AIAA Paper 2013–2083 (AIAA, Reston, VA, 2013), where time series of the wave-packet signatures are extracted at different streamwise locations. The experiment runs at $Ma = 0.6$ and $Re = 5.7 \times 10^5$. A thorough analysis is performed. Statistical tools are used to estimate the embedding and correlation dimensions that characterize the dynamical system. Input-output transfer functions are designed as control-oriented models; and for this special case, consistent with other recent studies, we find that linear models can reproduce much of the convective input-output behavior. Finally, we show how surrogate models can partially reproduce the nonlinear dynamics.

DOI: [10.1103/PhysRevFluids.2.094605](https://doi.org/10.1103/PhysRevFluids.2.094605)

I. INTRODUCTION

Following the early studies of Mollö-Christensen [1–3], a considerable body of work has been devoted to exploring the nature of organized motions that are observed in turbulent jets [4–8]. It was hypothesized early on that this component of the flow might be understood in terms of an instability of the turbulent mean [4,9–13], and the importance of such flow structures for sound radiation has been suggested in numerous studies [6,14–19].

It is only more recently, however, thanks largely to progress in theory, numerical simulations, and experimental diagnostics, that it has been possible to explore these hypotheses in a comprehensive manner. Exhaustive comparison of the results of theory with experimental measurements has confirmed that the average characteristics of coherent structures in turbulent jets are remarkably well described by solutions of the Navier-Stokes equations linearized about the turbulent mean [20–22]; these solutions are synonymous with globally stable modal solutions [23–25], which, physically, amount to hydrodynamic waves that are convectively amplified in the upstream region of the flow but become neutrally stable and then decay farther downstream. It is for this reason that they are referred to as “wave packets” [41]. An example of a modal solution, from Ref. [25], is shown in Fig. 1, where it is compared with a realization taken directly from the large eddy simulation (LES) [26] that provided the mean flow. The wave packets can be seen to comprise a hydrodynamic component, with an amplitude envelope as described above, and an acoustic component that takes the form of a directive beam radiating to shallow angles. Considering the Reynolds number of the jet, $Re = 1 \times 10^6$, and the fact that it issues from a nozzle with fully turbulent boundary layers, the

*onofriosem@gmail.com

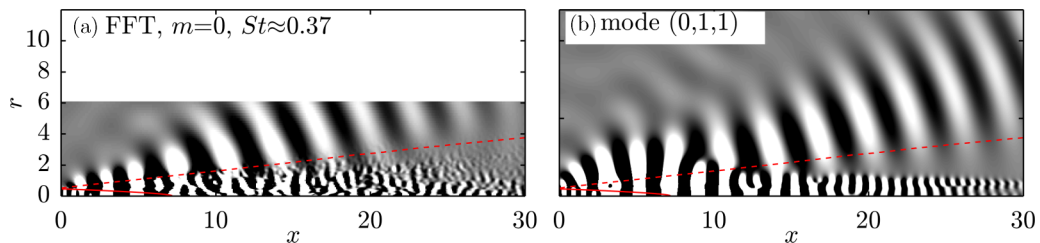


FIG. 1. Left: realization taken from large eddy simulation (axisymmetric component of pressure at $St = 0.37$). Right: Global mode $(m, St) = (0, 0.37)$. Courtesy of Ref. [25].

agreement between the LES realization and the linear global mode is striking. One is compelled to ask how, despite the nonlinear, orderless character of the turbulence that dominates the fluctuation energy of this flow, such organization can exist and how a linear model can capture so many of its features.

Something less clear from the images, however, is the considerably lower acoustic efficiency of the linear wave packet. As shown in a number of recent studies Refs. [22,27,28], the intensity of the sound field of the linear solution, once the hydrodynamic fluctuation levels of LES and model have been matched, can be as much as 40 dB below that of the LES. Such a large discrepancy, in the face of such compelling organizational similarity, is intriguing and the subject of a number of ongoing research efforts, which we summarize briefly in what follows.

The present understanding is that the linear dynamics do not contain the acoustically important degrees of freedom: The average wave packet does not generate the average sound [22,27,29–31]. The essential sound-producing motions are those associated with higher order statistics of the wave-packet dynamics. These motions have been denoted as “jitter” in Ref. [29] and would appear to be underpinned by nonlinearity [22,27,32,33]. Note that this applies in particular for subsonic jets, while in supersonic jets sound emission is less sensitive to jitter.

The nature of this nonlinearity remains to be clarified. Do wave packets jitter on account of nonlinear wave-wave interactions [34,35], or is it rather due to stochastic forcing of linear waves by background turbulence that leads to the activation of these higher order degrees of freedom [32,33]?

A useful conceptual framework for discussing these different scenarios, and which we will use throughout the paper when discussing the results, is that of an inhomogeneous linear system. In operator notation, $\mathcal{L}_{\bar{q}}\mathbf{q} = \mathbf{f}$, where $\mathcal{L}_{\bar{q}}$ is the Navier-Stokes operator linearized about the mean flow, \bar{q} ; the variable \mathbf{q} comprises wave-packet fluctuations and \mathbf{f} contains the nonlinear terms, usually discarded in a linear analysis but which are here retained and considered together as a forcing term. What this forcing term contains and what role it plays is, as discussed above, a question that many groups are presently trying to answer. Two hypothetical scenarios are as follows: (1) The nonlinear forcing term is dominated by wave-wave interactions and comprises thus some degree of order, or (2) it is dominated by stochastic turbulence interactions and is devoid of order. In order to facilitate discussion of the results, we will refer to these scenarios as involving, respectively, “endogenous” or “exogenous” nonlinear processes. Conceptually, wave packets are the flow objects that we are primarily concerned with, and the question is whether the nonlinear dynamics that underpins the jitter evoked above arises from endogenous wave-wave interactions or, rather, via forcing by a disorganized exogenous turbulence. In reality, of course, the forcing can never be truly exogenous, as it is an inherent part of the total flow. But, in the same way that one frequently appeals to a scale and energy separation between wave packets and energy containing turbulent eddies in order to justify use of the time-average mean as an equivalent laminar flow on which wave packets evolve, this *ad hoc* distinction between two kinds of nonlinear process is useful.

A further issue, that motivates both the modeling efforts evoked above and the work we undertake in this paper, is that of control. Given the success of linear models in predicting both the average wave-packet structure, in frequency space, and the real-time evolution in an experimental context [36], it is legitimate to ask if the tools provided by linear control theory might be sufficient. Such

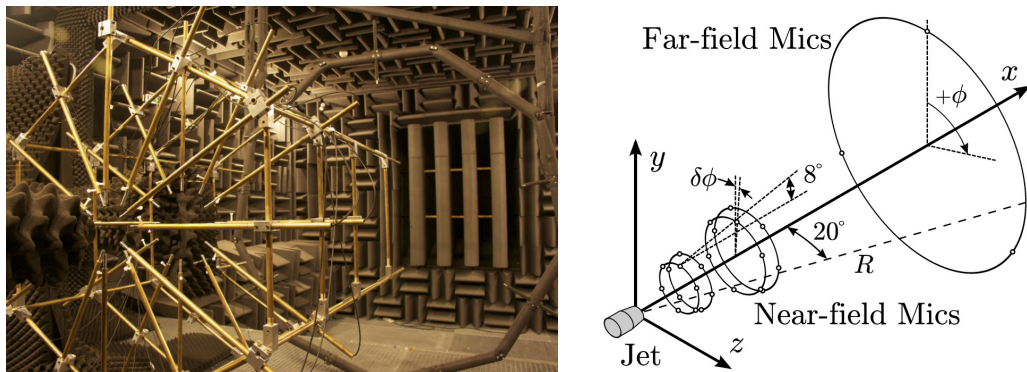


FIG. 2. Overview of the experiment, adapted from Ref. [39].

possibilities are presently being explored [37]. But if it were to be necessary to directly manipulate the more subtle dynamics associated with jitter (the energetically unimportant but acoustically essential degrees of freedom), then a nonlinear control framework would be required (machine learning, etc. [38]). The question of the dimension of the space spanned by the dynamics must be asked: Is this small enough for control to be realistic in an experimental context?

Consideration of the above issues via qualitative dynamical analysis has, to the best of our knowledge, not previously been attempted. We therefore consider the same turbulent jets studied by Refs. [21,39,40], using a variety of nonlinear signal processing and system identification techniques, in order to explore dynamics of low-frequency wave packets. Particular attention is given to pressure signals dominated by fluctuations at Strouhal numbers $St < 0.2$, where linear models are found to perform most poorly.

Our analysis starts with a brief description of the experimental setup in Sec. II. The remainder of the paper is organized in two parts. The behavior of the time series obtained from the experimental campaign is discussed in Sec. III, where statistical tools and spectral analysis are introduced for a preliminary characterisation of the temporal dynamics. In the second part, we pursue an alternative approach by analyzing reduced-order models of the time series, based on system identification; the approach is introduced in Sec. IV, while the dynamical analysis is reported in Secs. IV B and IV C. Further technical details of the techniques and data are provided in dedicated appendixes. Conclusions are summarised in Sec. V.

II. EXPERIMENTAL DATA

We consider an unforced, isothermal, subsonic jet issuing from a round nozzle with fully turbulent boundary layers. In particular, we consider the near-field pressure fluctuations measured by Ref. [39]. The setup is shown in Fig. 2(a), and a schematic of the near-field microphone array used for identifying the axisymmetric wave-packet signature is sketched in Fig. 2(b). The experiments were carried out in the anechoic free jet facility of the PPRIME Institute, Poitiers, France. The jet Mach number ranged from $Ma = 0.4$ to $Ma = 0.6$. In what follows, the diameter of the nozzle, $D = 0.05$ m, is taken as the reference length scale, while the exit velocity, U , is the reference speed. Time is scaled as $\tau = tU/D$. The corresponding Reynolds number $Re = \rho U D / \mu$ ranges between $4.2 \times 10^5 < Re < 5.7 \times 10^5$, where ρ is the density and μ the air viscosity. The end of the potential core of the jet is placed between $5 < x/D < 5.5$. Azimuthal rings of six microphones recorded pressure fluctuations from the near field of the jet, on a conical surface. Two data sets were analyzed.

(1) The first was obtained by simultaneous measurements at 7 different streamwise locations in the near field. At each location, an azimuthal ring, each with 6 microphones, is positioned. The array thus comprises a total of 42 microphones, placed on a conical surface in the near field of the jet, as shown in Fig. 2(b). The spacing between the rings is $x/D = 0.75$, within the range

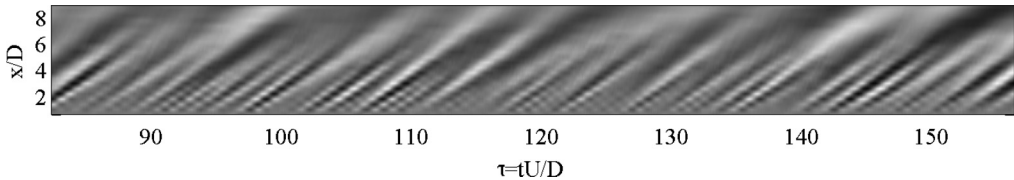


FIG. 3. The near-field signal is shown as a function of the distance from the nozzle exit (x/D) and the time τ , scaled with the velocity U and the diameter D . The measured quantity is the pressure related to the axisymmetric mode $m_\theta = 0$. The time series are obtained from the POD projection described in Ref. [39] and Appendix A.

$1.25 < x/D < 5.75$. At each x/D location, a Fourier-series decomposition is performed in the azimuthal direction.

(2) The measurements of the second campaign are performed using a ring of 4 equi-spaced, azimuthal rings, which are displaced in the streamwise direction over the range $0.5 < x/D < 8.9$ with a streamwise resolution of $x/D = 0.4$. These measurements are not simultaneous but allow computation of the cross-spectral-density matrix, an eigen-decomposition of which provides POD modes.

The POD basis is used for projection of the data from the first campaign. In Ref. [39], it is shown that much of the energy of the axisymmetric mode is captured in the first POD mode (up to 45–65%). The postprocessing and projection are detailed in Appendix A. The POD projection has some advantages, one of which is the provision of space-time information with a finer streamwise resolution and a larger streamwise domain. In what follows, the original time series is denoted *TS-Raw* while data projected onto the POD basis is denoted *TS-POD*.

The study focuses on the temporal dynamics of the axisymmetric mode $m_\theta = 0$. We study runs at $Ma = 0.6$ and Reynolds number $Re = 5.7 \times 10^5$, and consider different streamwise locations. We focus on the axisymmetric structures due both to their relevance for sound emission [40,41] and their dominance of the hydrodynamic near field where measurements have been performed; we further comment on this choice in the next section.

The analysis is carried out by considering *time series* extracted for each of the data sets. By definition, a time series is a sequence of equispaced data points, a function of time. The sample rate is 10^5 Hz, and the total number of points for each series is $N = 2.4 \times 10^5$. The temporal dynamics is shown in Fig. 3, as a function of time τ and streamwise position. This space-time picture is complementary to the frequency-space realization shown in Fig. 1. Both show clearly the organized nature of wave packets in these high-Reynolds-number, fully turbulent jets. We postulate that the near-field measurements provide a faithful signature of wave packets, which are radially extended flow entities, and particularly so where the pressure field is concerned. Indeed, the measurement in the near field provides a good measure of the dynamics inside the potential core of the jet (as shown in Fig. 1).

In the following section, analysis of the temporal series is performed by means of spectral analysis and estimation of the embedding and correlation dimensions.

III. PART I: TIME-SERIES ANALYSIS

We here consider the time series connected to the axisymmetric mode (*TS-Raw*) and the data is postprocessed by projecting on POD modes (*TS-POD*). The main goal is to characterise the time series from a dynamical-systems point of view. In principle, a dynamical system can be qualitatively analyzed by reconstructing the—unknown—underlying attractor from a sequence of observables of its state, for instance, the time series. This idea is at the heart of the Takens’s theorem [42], an embedding theorem providing the conditions under which the reconstructed dynamics preserve the properties of the original system and ensure a diffeomorphism between the hypothesized phase

space and the reconstructed phase space. The reconstructed dynamics is globally characterized by two geometrical properties:

(1) the *minimal embedding dimension* m , i.e., the dimension of the projection phase space of the reconstructed dynamics, and

(2) the *correlation dimension* d_2 , a measure of the fractal dimension of an attractor; see Ref. [43].

According to Takens's theorem, the correlation dimension d_2 is related to the embedding dimension m as

$$m \leq 2d_2 + 1. \quad (1)$$

We stress that although we are considering a fully turbulent jet at high Reynolds number, we are not directly probing turbulence but instead the dynamics of the wave packets. These entities carry only a small fraction of the fluctuation energy in comparison with the entire flow, despite their important role in the generation of sound [41]. Thus, we limit our analysis to the low-order dynamics underpinned by these structures, in the spirit of what has been suggested in Ref. [44]. Indeed, from a more physical point of view, it is the presence of such coherent structures that make this analysis relevant. A similar application is described in Ref. [45], where the presence of vortex pairing and large coherent structures in a transitional jets enabled a direct estimation of the correlation dimension.

A. Embedding and correlation dimensions: Definitions

The available time series are univariate; the embedding is thus the first step for the qualitative analysis. We rely on the classical approach: Choosing an embedding dimension m , each coordinate is obtained by a time delay Δt . From the time series, $y(t)$, the embedding vector is

$$\mathbf{Y}(m, \Delta t) = [y(T), y(T + \Delta t), y(T + 2\Delta t), \dots, y(T + m\Delta t)], \quad (2)$$

where T indicates the time span; note that the last channel will have a total shift of $m\Delta t$ with respect to the first one.

Once an embedding vector is obtained, we must identify the minimal embedding dimension m that allows determination of the dimension of the (hypothesized) attractor. A small m indicates the possibility of unfolding the attractor. A robust method for estimating the minimum embedding dimension is the *false nearest algorithm* [46]. Following the description given in Ref. [47], we can define the parameter a as

$$a(i, m) = \frac{\|y_i(m+1) - y_{n(i,m)}(m+1)\|}{\|y_i(m) - y_{n(i,m)}(m)\|}, \quad (3)$$

using the time series in Eq. (2) with $i = [1, 2, \dots, N - m\Delta t]$ and $\|\cdot\|$ being a measure of the Euclidian distance; note that the subscript $n(i, m)$ indicates an integer value such that $y_{n(i,m)}$ is the nearest neighbor of y_i .

Based on this definition, two points close in the m -dimensional space that are still close in the $(m+1)$ -dimensional space are called *true* neighbors; if this is not true then they are *false* neighbors. Embedding is achieved in the absence of false neighbors. The presence of false neighbors can be estimated using the parameter $a(i, m)$ in Eq. (3); details are provided in Sec. III C 1.

The second dimension of interest is the correlation dimension, d_2 , providing an estimate of the fractal dimension of an attractor. First, a correlation sum is defined as the fraction of all possible pairs of points $(\mathbf{Y}_i, \mathbf{Y}_j)$ closer than a given distance ε as

$$C(\varepsilon) = \frac{1}{N_p} \sum_{i=1}^N \sum_{j=i+1}^N \Theta(\varepsilon - \|\mathbf{Y}_i - \mathbf{Y}_j\|), \quad (4)$$

where Θ is the Heaviside step function and $N_p = N(N-1)/2$ is the number of pairs. The correlation sum $C(\varepsilon)$ contains only the pairs with a distance smaller than ε . The correlation dimension d_2 is

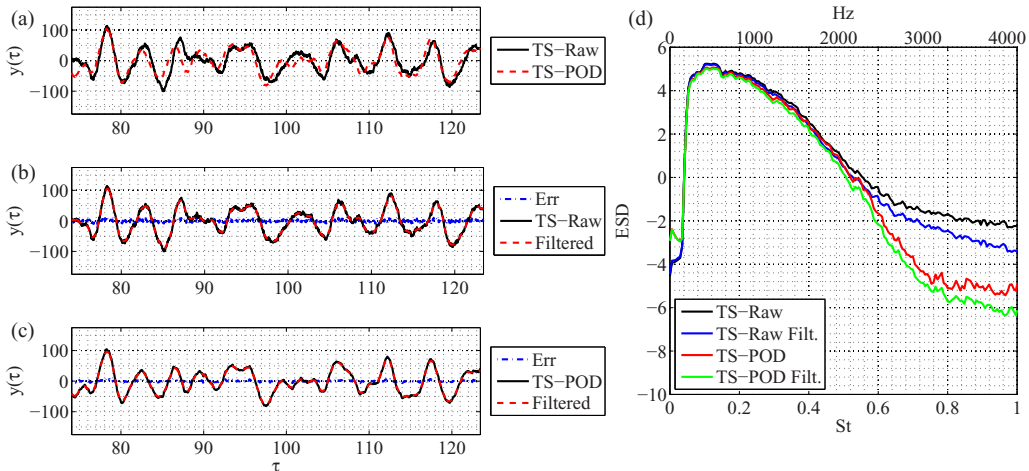


FIG. 4. Temporal behavior for the mode $m_0 = 0$ at $x/D = 5.7$. In the inset (a) the original signal (*TS-Raw*) is compared to the result of the POD postprocessing (*TS-POD*), at a location $x/D = 5.75$. A second nonlinear filter is applied to both the series as shown in the insets (b) and (c), where the original time series (black solid line) is compared to the POD-projected one (red dashed line); the resulting error is shown as a blue dash-dotted line. Finally, in the inset (d) the spectrum of the four time series is shown using the logarithm of the energy spectrum density (ESD) as a function of St . A difference between *TS-Raw* and the *TS-POD* is observed for $St > 0.6$, while good agreement is obtained at St numbers relevant for our analysis.

proportional to $C \propto \varepsilon^{d_2}$ and is estimated using the formula

$$d_2 = \lim_{\varepsilon \rightarrow 0} \lim_{x \rightarrow \infty} \frac{\partial C(\varepsilon, N)}{\partial \ln \varepsilon}; \quad (5)$$

see Ref. [43,46]. In what follows, we adopt statistical tools implemented by Kantz and Schreiber [46] and Cao [47].

B. Filtering and spectral analysis

We first perform nonlinear noise reduction. Indeed, noise is a limiting factor for the embedding procedure as it tends to increase the dimensions of the state space and reduces the reliability of the measurements [46]. The denoising algorithm is a moving-average filter, applied along the trajectory identified in the embedding space, on the assumption that the dynamics be continuous. In Fig. 4, the time series is shown at $x/D = 5.7$. In particular, we are interested in assessing to what extent the applied filters modify the essential dynamics of the time series.

In Fig. 4(a), the *TS-Raw* data are compared with the *TS-POD* set in the time domain. A quantitative assessment is reported in Fig. 4(d) using Welch's estimate. In the figure, the energy spectral density (ESD) is shown as a function of the St number; the energy spectral density is obtained from the power spectral density (PSD) estimate, normalized by premultiplying it twice with the rate of frequency sampling Δf . At the significant Strouhal numbers, $St = fD/U$, it can be seen that the POD projection does not strongly modify the dynamics of the time series. Differences can be observed only at $St > 0.55$ (where the data are dominated by acoustic rather than hydrodynamic fluctuations), while at lower St the cutoff is due to high-pass filtering of the original data applied to remove energy below the anechoic cutoff frequency of the wind tunnel. The two data sets are filtered using the nonlinear tools and results are reported in Figs. 4(b) and 4(c). By definition, the nonlinear filter does not act on specific bandwidths, but on the whole spectrum, while preserving the foliation of the attractor in the embedded space. Welch analysis confirms this behavior: In Fig. 4(d) we can observe that the nonlinear filter acts on the whole range of St numbers. The standard deviation

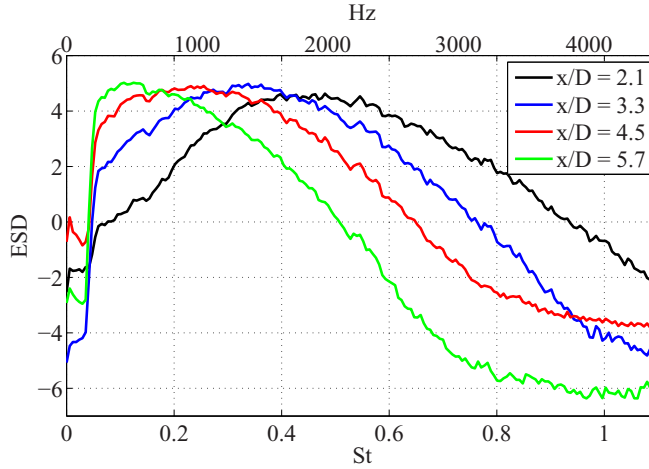


FIG. 5. Energy spectral density (ESD) as a function of St at different locations along x/D , namely $x/D = 2.1$, $x/D = 3.3$, $x/D = 4.5$, and $x/D = 5.7$. Only the series projected on the PODs are considered. It can be observed that the peak shifts from $St \approx 0.50$ to $St \approx 0.15$ when considering downstream locations.

of the removed noise is $\sigma = 0.075$ and $\sigma = 0.063$, for TS-Raw and TS-POD, respectively. The spectral content of the TS-POD data at $x/D = [2.1, 3.3, 4.5, 5.7]$ is compared in Fig. 5. We observe that the maximum fluctuation levels move progressively to lower frequencies as the observation position moves downstream, from $St \approx 0.50$ at $x/D = 2.1$ to $St \approx 0.15$ at $x/D = 5.7$. A change in the maximum amplitude can also be observed. A complementary analysis is provided by the spectrogram in Fig. 6(a) for the TS-POD at $x/D = 5.7$. All the spectrogram analyses contained in this paper are computed using the short-time Fourier transform (STFT), implemented in the MATLAB toolbox for signal processing. The graph is in two dimensions: The horizontal axis represents the time scale, while the St number is reported along the vertical axis. The amplitudes are shown as a color map of the PSD: At each instant, the intensity of the fluctuation is shown as a function of St . The Welch estimate can be regarded as an average along the time span of the results shown in the spectrogram. In particular, in Figs. 6(b) and 6(c), two instants are shown at $\tau \approx 170$ and $\tau \approx 240$,

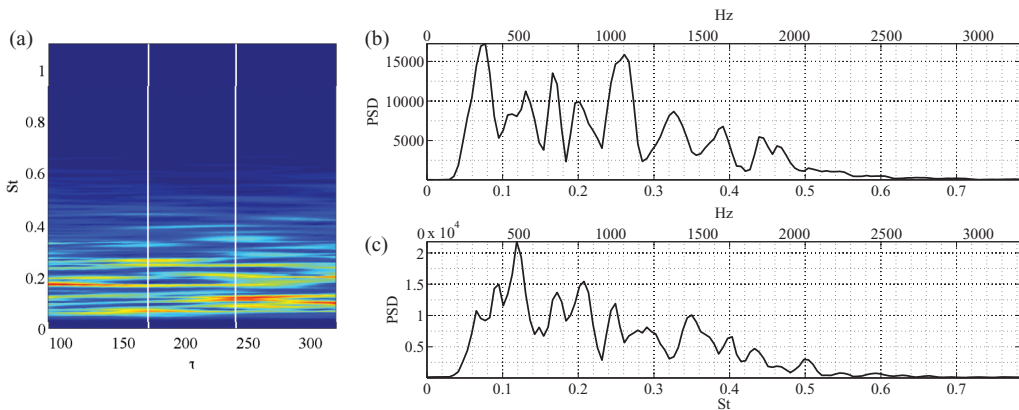


FIG. 6. Spectrogram for the time-series based on the POD projection at $x = 5.7$. In the insets (b) and (c), the power spectrum is shown as a function of the Strouhal number St at $\tau \approx 170$ and $\tau \approx 240$. Frequency in Hz is also reported.

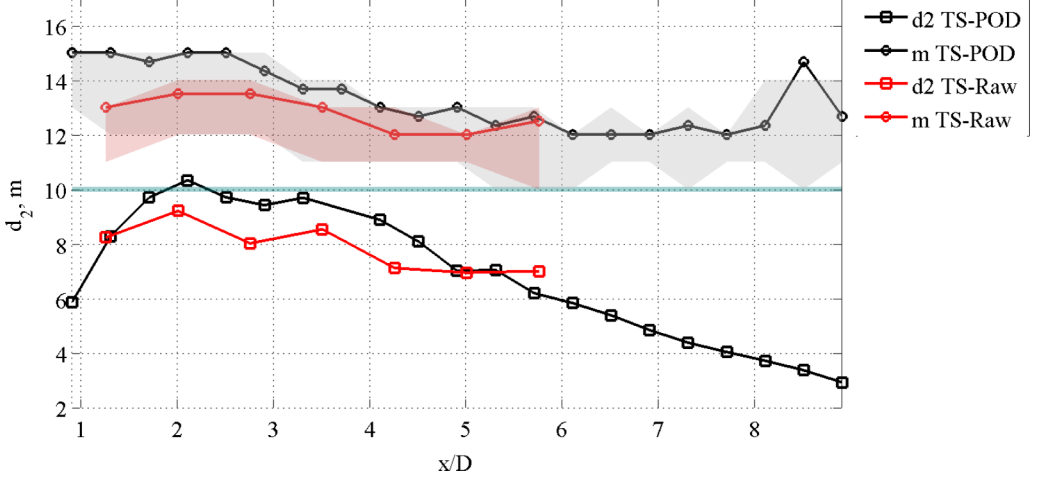


FIG. 7. The estimates of the embedding dimension m and the correlation dimension d_2 are summarized as function of x/D for both the datasets under investigation. The minimal embedding dimension m is computed for two different time delays, defining the confidence intervals indicated with shadowed areas: a smaller time of embedding, $\Delta t = 0.21$, defines the upper limit, while a longer time, $\Delta t = 0.29$, is related to the lower bound. The red area is obtained for the TS-Raw series, while the gray one is associated with the results of the dataset TS-POD. The nominal estimate for m (dotted curves) is obtained by averaging the results of different runs. The correlation dimension d_2 is indicated with a squared-dotted black curve and a squared-dotted red curve for TS-POD and TS-Raw, respectively. A green line indicates the Eckmann-Ruelle limit: Values of d_2 above this bound are not physical.

respectively. The instantaneous amplitudes of certain frequencies in the bandwidth can be observed; this behavior is a time-frequency view of the organized behavior manifest in space-time in Fig. 3. These behaviors are the signature of the amplifier nature of the flow: Wave packets are hydrodynamic instability waves that exist on the turbulent mean flow. The waves acquire initial amplitudes and phase at upstream stations—either from disturbances issuing from the turbulent motions within the nozzle or from distributed turbulence that acts as a volume force—and evolve in the downstream direction according to the stability properties of the linear operator, possibly subject also to distributed forcing, either from endogenous or exogenous forcing, as discussed in the introduction.

C. Embedding dimension and correlation dimension

The correlation dimension d_2 and embedding dimension m are computed for both TS-Raw and TS-POD data sets, filtered nonlinearly. The results are summarized in Fig. 7, where the two quantities are shown as a function of the streamwise direction x/D .

1. Minimal embedding dimension

The minimal embedding dimension m is estimated using the algorithm described by Cao in Ref. [47]. Starting from the parameter $a(i, m)$ in Eq. (3), the Cao function is defined as

$$e(m) = \frac{1}{N - m\Delta t} \sum_{i=1}^{N-m\Delta t} a(i, m). \quad (6)$$

This function corresponds to an average of $a(i, m)$ performed over the channels of the embedding vector \mathbf{Y} ; in this way, spurious evaluation of the embedding dimensions are avoided. The algorithm does not strongly depend on the length of the time series and it is capable of estimating the embedding dimension also for time series describing high-dimensional attractors. The method starts with low

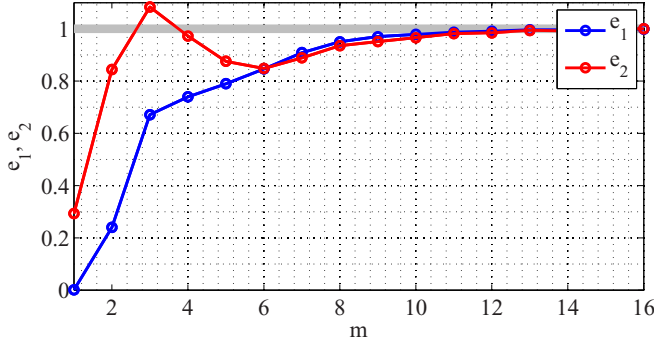


FIG. 8. Example of minimum embedding dimension m estimation. The POD-projected data are used, in $x/D = 5.7$. The saturation of the parameter e_1 (blue curve) indicates the minimal embedding m ; the complementary parameter e_2 (red curve) confirms the determinism of the dataset, as $e_2 \neq 1$ for $m < 13$.

values of m and proceeds by increasing m until the number of false neighbors decreases. The minimum embedding dimension m is estimated by analyzing the behavior of the parameter $e_1(m)$,

$$e_1(m) = \frac{e(m+1)}{e(m)}, \quad (7)$$

whose saturation indicates the minimal embedding dimension and is obtained for $e_1 \rightarrow 1$. In our case, we consider a threshold value $\delta = 0.99$. Cao's algorithm allows a clear determination of whether the signal is deterministic or stochastic, using

$$e_2(m) = \frac{e^*(m+1)}{e^*(m)}, \quad (8)$$

where

$$e^*(m) = \frac{1}{N - m\Delta t} \sum_{i=1}^{N-m\Delta t} |y_{i+m\Delta t} - y_{n(i,d)+m\Delta t}|. \quad (9)$$

As already mentioned, the operator $n(i, \cdot)$ indicates an integer value such that $y_{n(i,d)+m\Delta t}$ is the nearest neighbor of $y_{i+m\Delta t}$. Random series will be characterized by $e_2(m) = 1$, for any m . For deterministic data, e_2 cannot be constant.

Our computations provide the two values e_1 and e_2 estimated for each of the positions x/D . An example is shown in Fig. 8, where the TS-POD series is analysed in $x/D = 5.7$. We observe that $m = 13$, using e_1 ; more importantly, the values of e_2 are not constantly unitary: This is a first clue that we are analyzing deterministic time series.

A critical aspect is the choice of the embedding delay, Δt , and the number of samples. In principle, the embedding dimension, m , is independent of Δt ; in practice, the minimum embedding dimension estimate may depend on this choice and needs to be verified case by case. In Fig. 7, we identify a confidence interval for the m estimates; the upper bound corresponds to a time delay $\Delta t = 0.21$, while the lower bound is obtained for $\Delta t = 0.29$. The choice of the embedding delay is done by analyzing the autocorrelations. We verified that the estimated m is negligibly affected by the length of the series; for our computation, we considered $N = 1.0 \times 10^4$ points.

The confidence intervals are shown using shadowed areas. Each point corresponds to the value where the parameter e_1 saturates, as discussed in Fig. 8. Dotted curves identify the minimal embedding dimension computed by averaging the results obtained with $N = [1.0, 1.5, 2.0] \times 10^4$ points and $\Delta t = 0.21$. It can be observed that the TS-Raw series is characterized by a rather constant value of m , oscillating between a minimum value $m = 12$ at $x/D = 5$ and maximum

values $m = 13$ – 14 further upstream, at $x/D = 2$. This estimate follows closely the upper bound of our confidence interval. The lowest value is found at $x/D = 5.7$, for the runs at $\Delta t = 0.29$.

The TS-POD series provide higher values of both d_2 and m . This counterintuitive behavior is discussed in Sec. III D. For values $x/D > 5.7$, the minimal embedding dimension is practically constant until $x/D = 8$; however, note that in this region the data have been extrapolated.

2. Correlation dimension

The correlation dimension, d_2 , is estimated using the routines included in Refs. [46,48], based on the Grassberger-Procaccia algorithm; see Eqs. (4) and (5). A limit characterizes the computation of the correlation dimension; in particular, the value of the correlation dimension d_2 over a decade cannot exceed $d_2 = 2\log_{10}N$, where N is the number of points in the time series (Eckmann-Ruelle limit [49]). The amount of data available allows us to get a value of $d_{\max} \approx 11$. This means that when we approach this upper bound, it is not legitimate to conclude that the d_2 value corresponds to the dimension of the inner dynamics. Moreover, a consistent estimation of the correlation sum C should cover a random sample of independent pairs: In the time series, successive elements are generally not independent and can be highly correlated. To limit this effect, which could lead to inconsistent results, a time shift indicated with T_w —the Theiler window—is introduced to reduce the correlation between points during the pair counting. The N_p pairs are chosen as

$$N_p = (N - m)(N - m - T_w - 1)/2 \quad (10)$$

in Eq. (4). In this way, we discard all pairs of points whose time indices are less than T_w , avoiding the oversampling.

Convergence tests were performed over the input parameters of the algorithm: the range ε , the embedding quantities m , the time delay, and the Theiler window. In Fig. 7, the results are shown with squared-dotted curves. For each of the positions considered, we analyzed two subsequent blocks of data containing a total of $N = 10^5$ points; thus, only values of correlation dimension, $d_2 < 10$, are considered relevant (a green shadowed area indicates the limit). The final value of d_2 is obtained by averaging the results of the blocks. We observe that the time delay, Δt , imposed for the embedding procedure does not influence the final result. A Theiler window of $T_w \approx 0.4$ was chosen; we do not observe significant changes on increasing this parameter.

For the series TS-Raw, we observe a behavior similar to m , with $7 \leq d_2 \leq 9$ in the span $1.25 \leq x/D \leq 5.75$. For the TS-POD, consistent with the previous estimate of m , we found that the values of d_2 are slightly higher. In the upstream region, $x/D \approx 2$, the value close to the upper bound $d_2 \approx 10$ does not allow us to conclude that this is the effective value of the correlation dimension. However, the dimension d_2 with respect to the embedding dimension m is bounded by the limits imposed by Takens's theorem.

A decrease is observed in the vicinity of the nozzle $x/D < 1$ and far downstream in the extrapolated region, $x/D > 6$, where important dynamics have been suppressed by the projection and extrapolation (see Ref. [39]).

D. Estimated dimensions: A brief discussion

The preliminary analysis of the minimal embedding dimension m and the correlation dimension d_2 indicates deterministic behavior, despite the limitations that both algorithms pose. Interestingly, the values of m and d_2 are higher when considering the POD-projected data. This result has been found also by computing the embedding dimension with a different version of the *false nearest* strategy (results are not reported). We believe that the behavior may be due to the physics educed by the measurement procedure, rather than to a numerical artefact. As mentioned in Sec. II, the simultaneous pressure measurements of TS-Raw are projected on a POD basis obtained using two-point flow statistics obtained using a larger number of more finely spatially resolved points. Our working hypothesis is that projection on the more finely resolved POD basis leads to the eduction of a richer dynamics, due to the greater finesse of the educed two-point wave-packet structure.

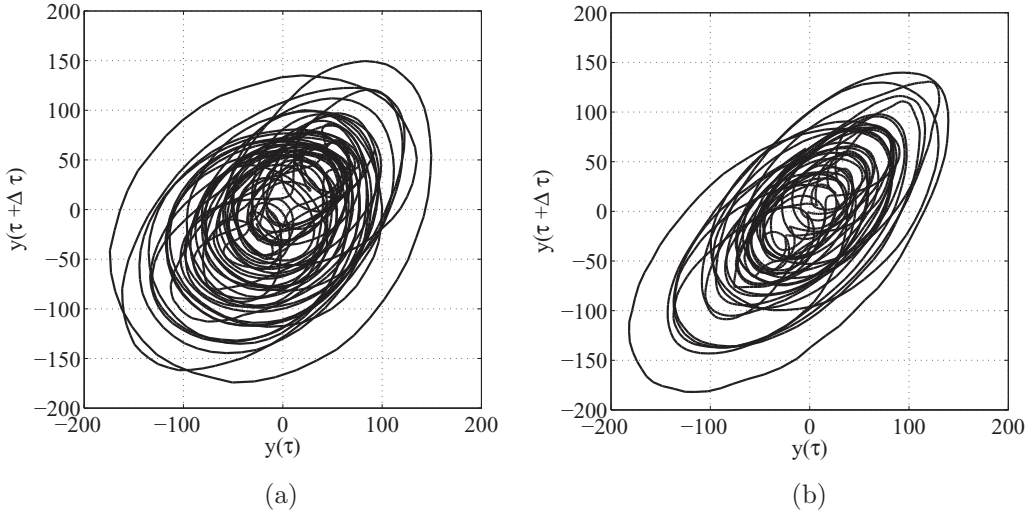


FIG. 9. Phase-space projection for two positions taken from the TS-POD series. The embedding space is obtained by time-delayed coordinates, using $\Delta t \approx 0.4$. (a) Phase space, $x/D = 2.5$ and (b) Phase space, $x/D = 4.1$.

On the other hand, for $x/D \geq 5.75$, we observe a rather low correlation dimension and a constant embedding dimension until $x/D \approx 8$. We attribute this effect, as discussed earlier, to the extrapolation of the data in this region of the flow resulting in a fictitious low dimensionality of the system. For this reason, in the following sections we focus only on the points $x/D < 5.75$.

The embedding space that should be used according to the Takens criterion is rather large. In Figs. 9 and 10(a), we show three phase portraits reconstructed in a three-dimensional embedding space obtained by imposing a delay of $\Delta t \approx 0.4$, between each of the three coordinates. In all cases, at a first glance, the reconstructed phase space suggests a toroidal nature for the dynamical

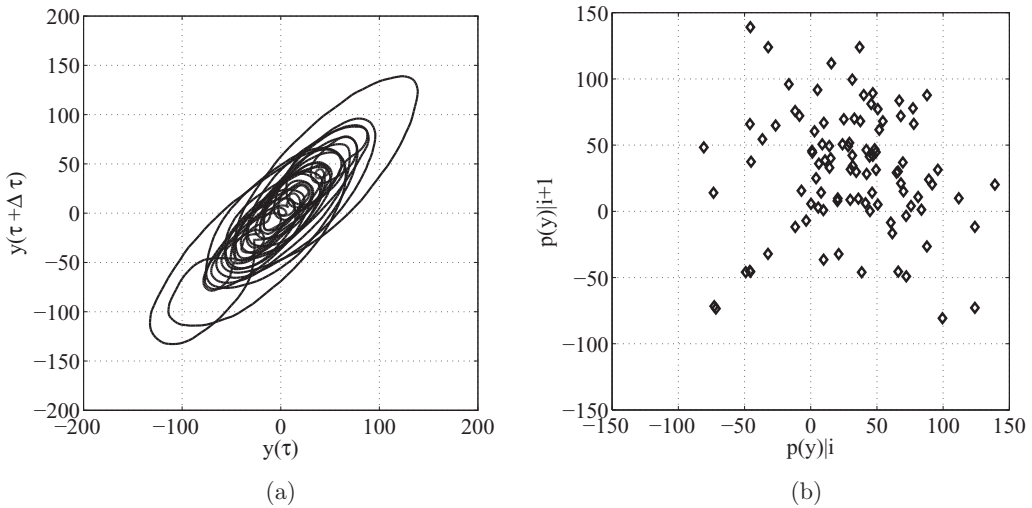


FIG. 10. Phase-space projection for the TS-POD series at $x/D = 5.7$ (left) and first return map obtained by stacking the local peaks of the time series. The embedding space is obtained by time-delayed coordinates, using $\Delta t \approx 0.4$. (a) Phase space, $x/D = 5.7$ and (b) First return map, $x/D = 5.7$.

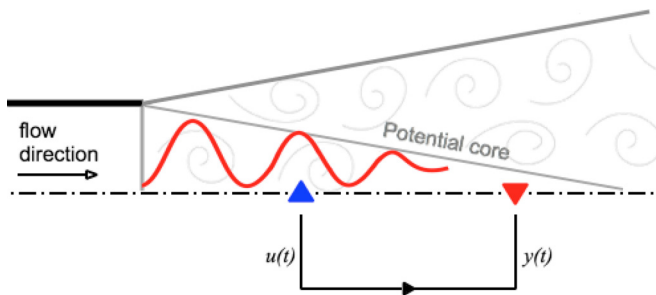


FIG. 11. Sketch of a input-output system adapted to the jet configuration analyzed in the paper. The input u is indicated by a blue arrow, while a red symbol indicates the output y . These elements are contained within the potential core length. As explained in Sec. II, we consider the dynamics related to the coherent axisymmetric waves, graphically indicated with a red solid line. The connection between the input and the output indicates a transfer function between them.

system; unfortunately, the projection is poor due to the high dimensionality and cannot be further investigated. Moreover, the first return map in Fig. 10(b) suggests contamination of the dynamics due to exogenous processes. Similar results were obtained for all the positions along x/D regardless of which embedding strategy was used (Singular value decomposition embedding and derivative embedding). In other words, although the embedding and correlation dimensions are consistent with determinism of the time series and suggest that the dynamics is relatively low dimensional, their values are still too large for useful characterization of the attractor geometry.

Finally, note that the strong spatiotemporal organization characterizing $m_\theta = 0$ is also observed in single-point measurements, because of the aforesaid dominance of the axisymmetric mode in the near field. This observation leads us to believe that analysis of the $m_\theta = 0$ dynamics is appropriate for education of the essential dynamics.

IV. PART II: SYSTEM IDENTIFICATION FOR CONTROL AND MODELING

The preliminary study of the time series based on statistical tools and Fourier analysis suggests that the underlying temporal dynamics of the axisymmetric coherent structures is deterministic. However, the dynamics deduced locally is rather rich and cannot be analyzed by simply using the standard tools from dynamical system theory. For this reason, we resort to *system identification*, which aims at building mathematical representations of dynamical systems from set of observables, i.e., measured data. This approach can also be useful for the provision of control-oriented models.

The problem is shown schematically in Fig. 11 where we introduce inputs and outputs, graphically indicated as blue and red markers, respectively. In the following, the variable (or output of the system) will be denoted by the scalar-valued vector $y(t)$ and will be represented by the measurements taken at different streamwise locations. The inputs will be indicated by the vector $u(t)$.

In the last ten years or so, system identification has been extensively used in fluid mechanics, mainly for control purposes (see Refs. [50,51]). Such applications consist in identifying reduced-order models that describe the input-output behavior, between $u(t)$ and $y(t)$. On the other hand, in an effort to understand the underlying dynamics of the system, one can also identify surrogate models that reproduce the dynamics of the system (or part of it) by statistical inference based solely on the outputs $y(t)$ [46,52]. As will be shown in the following, the two tasks are rather different, although they share the same tools.

The basic model we consider consists of nonlinear Volterra series of polynomials, written as

$$y(t_n) = \sum_{i=1}^{n_\alpha} \alpha_{n-i} y(t_{n-i}) + \sum_{i=1}^{n_\beta} \beta_{n-i} u(t_{n-i}) + NL[u(t), y(t)] + e(t_n). \quad (11)$$

This relation is called the *equation error model*. On the right-hand side, the first term relating the past outputs with the present $y(t)$ is referred to as the *autoregressive* term; the second term reproduces the dynamics between the inputs $u(t)$ and the outputs $y(t)$ (*exogenous* part). The unknowns of the model are the set of coefficients α , β , the coefficients of the non-linear part (here represented by high-order polynomials), and the error $e(t)$.

In this section, we will refer to *noise* as indicating the external forcings driving the system dynamics. As already said, turbulent jets are convectively unstable, so strongly sensitive to external forcings; *measurement noise* will be generally indicated as *error* or *residual* in the context of the identification problem and modeled or extracted with the variable $e(t)$. A classical way to model the error $e(t)$ is to consider it as a *moving average* of unknown white noise. The resulting algorithm for the identification of the unknowns of the equation error model 11 is the nonlinear (N) autoregressive (AR) exogenous (X) with moving average (MA) algorithm, usually referred as N-ARMAX. An overview of the algorithm is provided in Appendix B, while for a deeper discussion we refer to Refs. [53–55].

A. Identification of the models and choice of the inputs

We start from the hypothesis that our observables properly represent a relevant part of the jet dynamics; the hypothesis is corroborated by numerous companion works on the stability analysis of the wave packets associated with these temporal series (see Refs. [21,41,56,57]). The identification procedure involves numerous parameters that need to be evaluated; first, we choose the polynomial structure based on Volterra series and identify the unknowns (namely the coefficients) using the NARMAX algorithm (Appendix B). The second step is the *model validation*: Among all the possible models, only a few allow a proper characterization of the dynamics. The validation is necessary in order to discard the models unable to reproduce a dynamics close to the real one; we list the main parameters of the validation procedure in Appendix C. Finally, the model is available for prediction and/or dynamical-systems analysis.

A distinction can be made here between *nonautonomous* and *autonomous* models:

(1) Nonautonomous models are driven by the inputs $u(t)$; when the inputs are correlated with the outputs $y(t)$, most of the dynamics will be contained in the inputs themselves. In this case, the model will result in an optimal transfer function between these elements (see Fig. 11); we will refer to this approach also as *input-output* system identification. This approach is control oriented.

(2) Autonomous models are obtained when the exogenous (X) part represented by the input $u(t)$ is neglected. The algorithm used for the identification is the ARMA. The approach is also referred to as *output-only* system identification and it relies on partial information: In this case, the system is not arbitrarily driven and/or the input cannot be measured. The dynamics of the system is represented by the autoregressive (AR) part of the model.

In the following, we identify transfer functions (i.e., input-output models) that minimize the prediction error in terms of best mean-squared errors over a time horizon, given a measurement as input, $u(t)$ (Sec. IV B). Moreover, we attempt to characterize the dynamical mechanisms at work using nonlinear, output-only ARMA models in Sec. IV C. We will consider the TS-POD at $x/D = 5.7$, nonlinearly filtered (see Sec. III B). The TS-POD series are less affected by measurement noise, in the range where the simultaneous data from TS-Raw are available; moreover, the nonlinear filter preserves the dynamics across all the frequencies. The chosen locations for the outputs correspond roughly to the end of the potential core. All the models discussed in the next sections are computed using the tools developed by Aguirre and coworkers (see Ref. [52]). The linear limit was cross validated with in-house scripts [55].

B. Nonautonomous models: Transfer functions for control design

When the input term $u(t)$ is highly correlated with the output $y(t)$, the model obtained by applying system identification will represent a transfer function (cf. Ref. [36]). Because of the

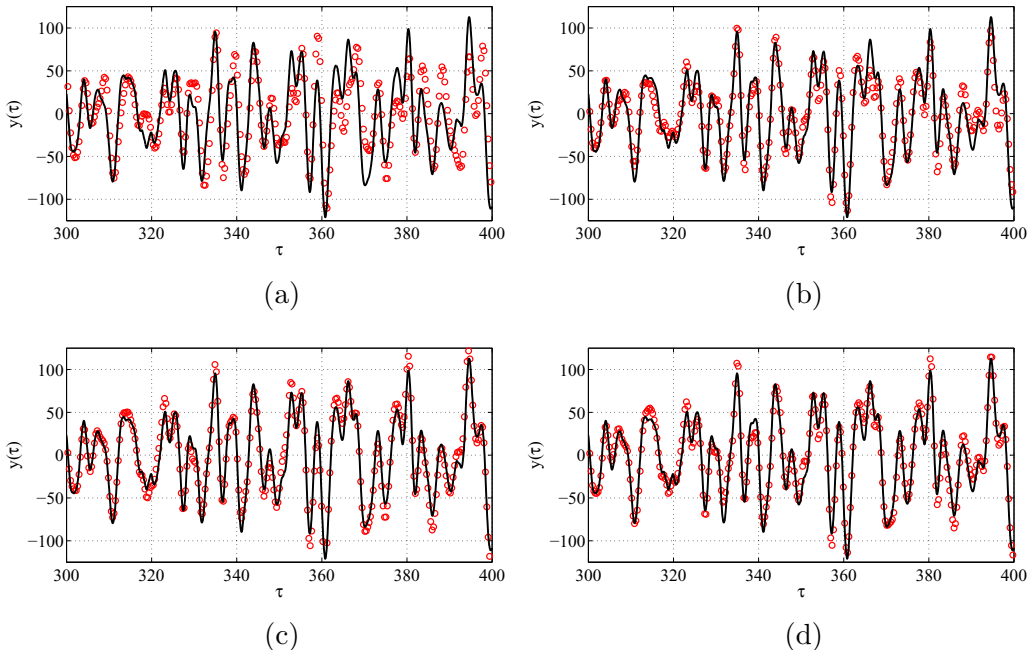


FIG. 12. Reduced-order model vs. original time-series. Solid, black lines indicate the original signal at $x/D = 5.7$; the red dots indicate the prediction based on the identified linear filter. Four inputs are considered, at $x/D = [2.5, 3.3, 4.1, 4.9]$. (a) Input $\mathbf{u}(\tau)$ at $x/D = 2.5$, (b) Input $\mathbf{u}(\tau)$ at $x/D = 3.3$, (c) Input $\mathbf{u}(\tau)$ at $x/D = 4.1$, and (d) Input $\mathbf{u}(\tau)$ at $x/D = 4.9$.

convective nature of the flow, we consider a setting where the inputs are upstream of the outputs, as in Fig. 11. We use the output at $x/D = 5.7$ and assume as input terms $\mathbf{u}(t)$, the outputs being placed at four different positions, $x/D = [2.5, 3.3, 4.1, 4.9]$. The models include only one input at each time (single-input-single-output, SISO). The time series resulting from the simulations are compared with the original time series in Figs. 12(a)–12(d). The window of assimilation is $t \in [0, 164]$. The validation is performed by integrating the model in the window $t \in [0, 620]$.

The application of the full nonlinear ARMAX algorithm results in fully linear models (similar to those obtained by Ref. [36]), based on a limited number of coefficients α and β , $N_\alpha = N_\beta = 20$. As will be further explained later, the linearity of the filters is not an *a priori* choice, but it is a result of the chosen optimization procedure.

We introduce as parameters for the performance assessment the normalized root-mean square defined as

$$e_y(t) = \frac{1}{A} \left[\sqrt{\frac{1}{N} \sum_{i=1}^N (y_i - \tilde{y}_i)^2} \right], \quad (12)$$

where $\tilde{y}(t)$ indicates the signal obtained from the linear filter driven by the input $\mathbf{u}(t)$. The parameter is scaled using an estimate of the signal amplitude $A = [\max(y) - \min(y)]$. Note that $\tilde{y}(t)$ is computed by running a 1-step-ahead prediction: Indeed, we rely on knowledge of the input in the previous $[1, 2, \dots, N - 1]$ steps. In Fig. 13(a), the results are summarized for a number of outputs along the streamwise direction. In particular, six different positions along x/D are introduced as inputs, in the range $2.9 \leq x/D \leq 4.9$, while as outputs are considered the locations downstream of the inputs between $x/D = 3.3$ and $x/D = 5.7$. For transfer functions with inputs at $x/D = 2.9$ – 3.3 and output at $x/D = 5.7$, a standard deviation, $e_y(t) \approx 0.05$ – 0.08 is observed; for all other cases, $e_y(t) < 0.04$.

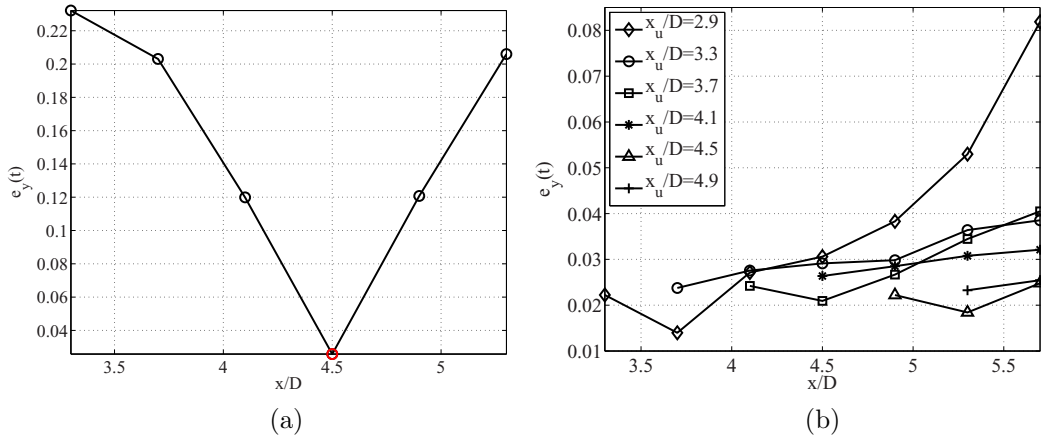


FIG. 13. Left: The normalized root mean square $e_y(t)$ between the models and the time series is analyzed. The x axis indicates the location of the output, while in the legend the six lines correspond to the inputs. In total, 27 models are analyzed, most of which are characterized by a standard deviation $\sigma < 0.25$. Right: The model is computed between the input at $x/D = 4.5$ and the output at $x/D = 5.7$; the same model, is tested by using different inputs between $x/D = 3.3$ and $x/D = 5.7$; the test shows the lack of robustness with respect to the time delays of the system. (a) Models' performance and (b) Robustness.

The linear models are found to perform well. As discussed earlier, in the presentation of the spectral analysis (cf. Fig. 5), the convective nature of the flow implies a progressive drift of the main frequency of amplification and a slight variation of the maximum amplitude in the spectrum as we move further downstream. In this sense, with a limited number of degrees of freedom it is possible to describe the modulation of amplitudes and frequencies, and the time delays associated with convection. The result confirms and extends those obtained by Ref. [36], where linear ARMAX modeling, parabolized stability equation (PSE), and empirical transfer function were compared for the estimation of downstream-propagating wave packets. With respect to Ref. [36], in our analysis the linearity of the model is a result of the optimization process and not a working hypothesis. The candidate models introduced in the identification procedure were nonlinear and characterized by all the terms of Eq. (11) up to order $n = 3$. The identification procedure makes use of the orthogonal least-squares (OLS) algorithm; see Ref. [58]. This iterative scheme ranks the terms of the initial candidate model according to their relative importance and discards those that contribute negligibly to approximation of the initial time series. We found that the nonlinear dynamic terms are relatively unimportant for an optimal representation of the convection-dominated transfer functions; thus, linear modeling is found to be sufficient for characterization of the input-output behavior of the system.

1. Discussion: Robustness and control design

The good performance of the linear models has interesting implications for the control design. In particular, with respect to the convective nature of the flow, feed-forward control strategies can be envisaged, with self-tuning and adaptive controllers being used to deal with model uncertainties. Indeed, special attention must be paid to the robustness issue: The transfer functions only retain information regarding the time delays of the system, the modulation of the amplitude and the frequency bandwidth; moreover, the set of coefficients is obtained as a least-squares solution from the assimilation datasets at a given amplitude. As an example, in Fig. 13(b), we illustrate the lack of robustness with respect to time delays, due to the convective time of propagation of the perturbations. The model assimilated using the input at $x/D = 4.5$ is applied with different inputs, taken in the range $3.3 \leq x/D \leq 5.3$. The validity of the models quickly deteriorates.

A lack of robustness can be compensated for using different strategies. Control design can be conceived that can deal with robustness issues arising from uncertainties of the system, either using techniques from the robust-control framework [51] or from adaptive control theory [59]. The latter strategy is particularly well suited for convective flows. Adaptive controllers are characterized by two time scales: a *fast* time scale, for the real-time estimation of the input $\mathbf{u}(t)$, and a *slow* time scale, based on feedback measurements of the flow necessary for correcting off-design conditions. Examples of these strategies can be found for weakly nonlinear transitional flows [60] or nonlinear, turbulent cases [61].

Finally, note that the linearity of these models allow us to isolate azimuthal Fourier modes, although input-output estimation based on linear transfer function can also successfully predict the downstream behavior when the signals are characterized by fully three-dimensional test cases (see Refs. [59,60] and citations therein). In either cases, our choice of restricting the analysis to the axisymmetric mode does not lead to loss of generality where control-oriented modeling is concerned.

C. Autonomous models: Qualitative dynamics of the observables

In this section, we consider nonlinear autoregressive modeling with moving average (N-ARMA). With respect to the equation error model in Eq. (11), we neglect the exogenous terms (X) and consider the following basic model:

$$y(t_n) = \sum_{i=1}^{n_\alpha} \alpha_{n-i} y(t_{n-i}) + NL[y(t)] + e(t_n). \quad (13)$$

The model is autonomous and based solely on the output $y(t)$. The algorithm described in Appendix B identifies the number of necessary terms and coefficients $\boldsymbol{\alpha} = (\alpha_1, \alpha_2, \dots, \alpha_{n_\alpha})$; the unmodeled part is accounted for in the error term $e(t)$.

Note that output-only models have to rely on partial information. Known inputs, decorrelated from the outputs, maximize the information educed in the identification process; indeed, a true external stochastic input would improve the identifiability of the system and the quality of the regression method and allow exploring in a systematic way the state space. An optimal choice is represented by inputs modeled as stochastic white noise or random binary sequences. This third choice will be subject of future work, based on an *actuated* experiment where the dynamics is forced: Here, we pursue an alternative path. In particular, we aim at computing models that optimally represent a portion of the dynamics of the system within narrow windows of assimilation, with the idea of probing short flow cycles that are difficult to identify on account of the jitter discussed earlier, and in the spirit of the observations of [4]: “three or four puffs form and induct themselves downstream, an interval of confused flow ensues, several more puffs form, and so on” (p. 556). Following this reasoning, the limitations imposed by the N-ARMA applied to our dataset are circumvented by only focusing on the dynamics that can be properly analyzed by means of these tools, i.e., the short-lived events.

1. Selection of the models

The selection of the most appropriate models is performed in two steps: First, we compute a large number of them by varying the parameters defining the N-ARMA approximation. A brief discussion is included in Appendix C. During this step, the algorithm minimizes the error between the original series and the model within the assimilation window by applying a 1-step prediction. As a result of the parametric analysis, we identified a total of 36 000 models.

Once the models are available, we apply a temporal simulation not driven by known inputs, based on the N -step prediction; thus, when the simulation is performed on a longer time horizon, the nonlinear models quickly deviate from the original time series after a short transient roughly corresponding to the initial conditions. For this reason, it is also important to extract the spectral features. Because of the short time window of assimilation, we apply a power spectral density

estimation based on the Yule-Walker method [62], implemented in the MATLAB signal processing toolbox. This method estimates the spectral content by fitting an autoregressive linear prediction filter to the signal. By doing this and then comparing the results, we can discard models that are badly conditioned or unstable. Around 21% of the models show periodicity, quasiperiodicity, toroidal features, or chaotic behavior. Thus, despite the large number of initial candidates, after the validation, we finally retain ≈ 100 models, belonging mainly to three families. With families, we indicate cluster of models characterized by a comparable polynomial structure and coefficients behaving in similar manner from the qualitative point of view. We picked up three representative examples. For each of these, we discuss a representative model, labeled as follows

(1) *Model T*: In Fig. 14 the model is characterized by $n_\alpha = 26$. It is a toroidal (T) example that settles on the frequencies characterising the windows of learning.

(2) *Model LC*: In Fig. 15 the model is characterized by $n_\alpha = 25$. After a rather long transient (up to $\tau \approx 150$), it ends up on a stable limit cycle (LC); see Fig. 16.

(3) *Model S*: In Fig. 18 the model is characterized by $n_\alpha = 6$. It is a chaotic model, as can be seen from the first-return map. We believe that it reproduces some short (S) time dynamics related to the jittering.

The first two cases are characterized by a long window of correlation n_α . The third model is obtained considering the shortest possible correlation length. In the following paragraphs, we comment on their relevance from the phenomenological point of view.

2. Models T and LC

In Fig. 14, the properties of the model *T* are analyzed. As already mentioned, none of these models are predictive: After a short time, the dynamics quickly deviate from the original one [Fig. 14(a)]. However, the system is characterized by high sensitivity to noise, while the model behavior is dictated by the endogenous dynamics educed during the assimilation process. The quality of the model can be assessed by analyzing the spectral properties in the window of assimilation: In Fig. 14(b), the power spectral density is shown based on autoregressive modeling; the model reproduces the peak frequency $St = 0.25$; a second peak appears at $St \approx 0.35$. However, we can also observe that model *T* is not properly reproducing the low frequencies $St \rightarrow 0$. The long-time behavior is characterized by a toroidal behavior in phase space, shown with a red solid line in Fig. 14(d). The Fourier analysis in Fig. 14(c) and the first-return map built with the relative maxima in Fig. 14(e) confirm the phase space representation. In particular, in Fig. 14(e), the black dots correspond to the beginning of the trajectory, while the superimposed blue dots show the final part.

Model *T* is characterized by a limited match in the autoregressive PSD; for this reason, a second model is presented in Fig. 15, labeled as model LC. In this case, we observe a good agreement at low Strouhal numbers, $St < 0.5$ [see Fig. 15(b)]. We note a rather different behavior when comparing the transient with the asymptotic state. During the transient, the spectrum is not characterized by distinct frequencies [see Fig. 15(c)], although we observe the dominance of frequencies around $St = 0.35$ and $St = 0.15$ (due to the assimilation windows). The overall dynamics is more complex as shown in the phase-space portrait in Fig. 15(d); the corresponding first-return map in Fig. 15(e) can be understood by considering the long-time behavior of the system reported in Fig. 16. Indeed, after a transient of $\tau \approx 150$, the model settles on a limit cycle [Figs. 16(a) and 16(b)]; the dominating frequencies in Fig. 16(c) are the same as those observed in the Welch PSD analyzed in Fig. 15(c). Having the long-time behavior in mind, it is easier to understand the first-return map in Fig. 15(e). In particular, the blue dots are representative of the limit-cycle trajectory: We can observe that the model during the transient progressively settles on the limit cycle that “attracts” the trajectory.

The transient has a qualitative behavior similar to the original model also if observed from the spectrogram. In Fig. 17, it is possible to compare the original time series [Fig. 17(a)] with the model [Fig. 17(b)], in the same time span. It is evident that on average the length of the organized events is similar, while a significant difference is seen in the spectral energy distribution. As already discussed, this feature is an attribute of the exogenous dynamics at work on the dynamical system.

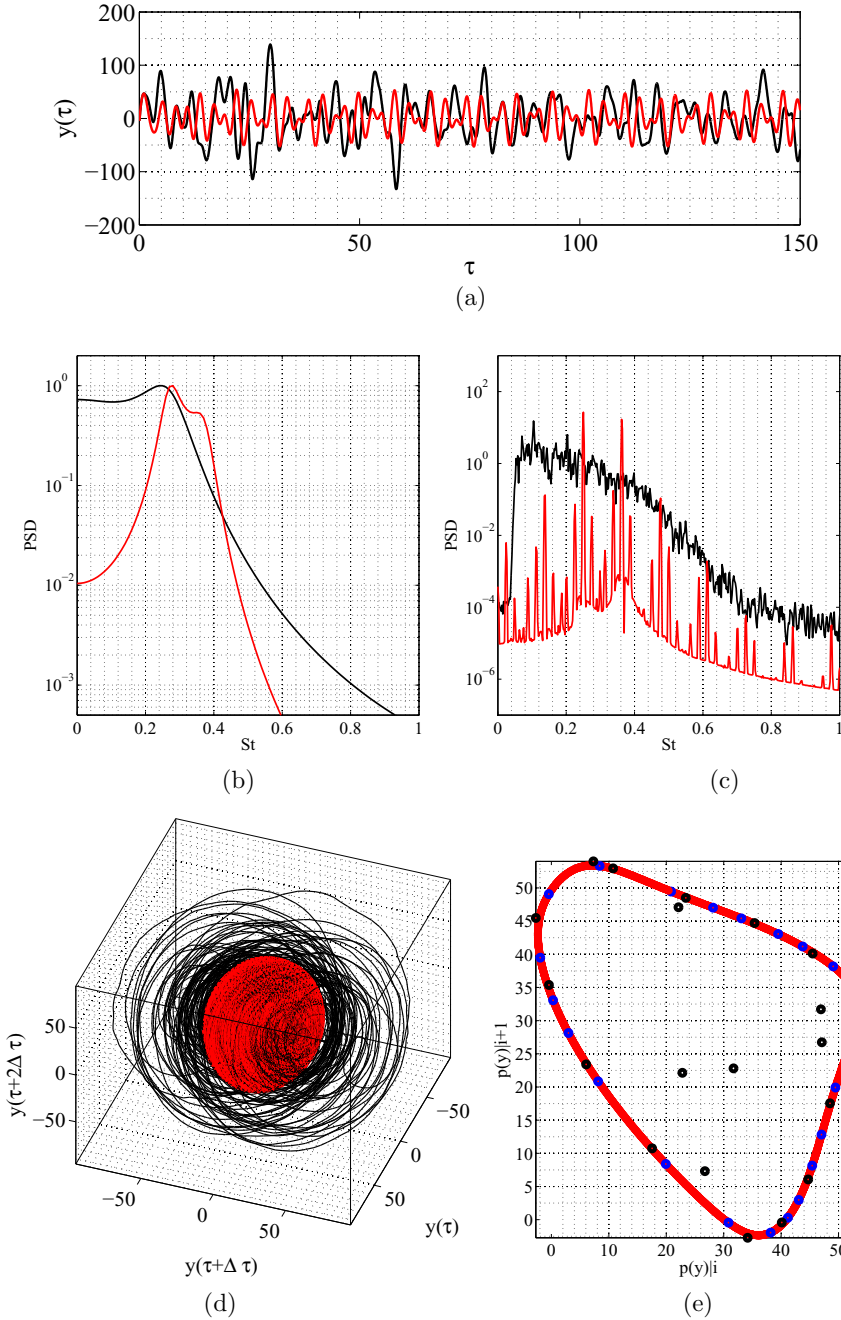


FIG. 14. Comparison between N-ARMA model T (in red for all the insets) and original time series TS-POD at $x/D = 5.7$ (in black). The surrogate data are obtained by integrating the model in time. The comparison in time domain (a) is only qualitative. Spectral analysis [(b), (c)] and phase-space reconstruction provide a more quantitative assessment of the performance of the model. The embedding space for the phase space reconstruction (d) is obtained with a delay $\Delta t \approx 0.3$. The first-return map is obtained using the maximum values in the model (e); the black dots correspond to the beginning of the trajectory, while the superimposed blue dots show the last points of the simulation.

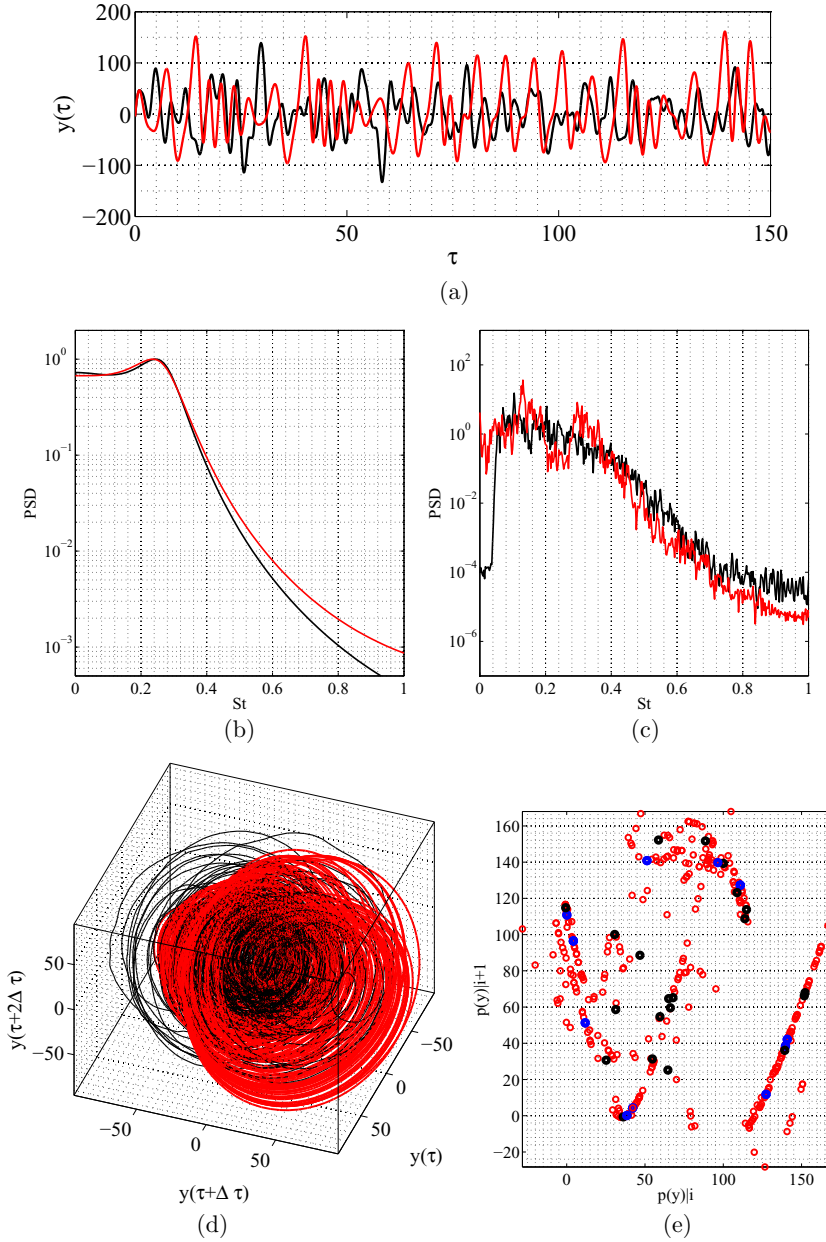


FIG. 15. The comparison between the data obtained from the N-ARMA model LC (in red for all the insets) and the original time-series TS-POD at $x/D = 5.7$ (in black) is shown in panel (a). Spectral analysis and phase space reconstruction are shown in panels (b) and (c). The embedding space for the phase space reconstruction (d) is obtained with a delay $\Delta t \approx 0.3$. The first-return map in the model (e); the black dots correspond to the beginning of the trajectory, while the superimposed blue dots show the last points of the simulation.

These two models suggest that if only the endogenous dynamics were considered, the dynamics due to nonlinear interactions among wave packets would be dominated by the organised behavior that characterizes the short-lived events observed in the spectrogram. In particular, the dynamics

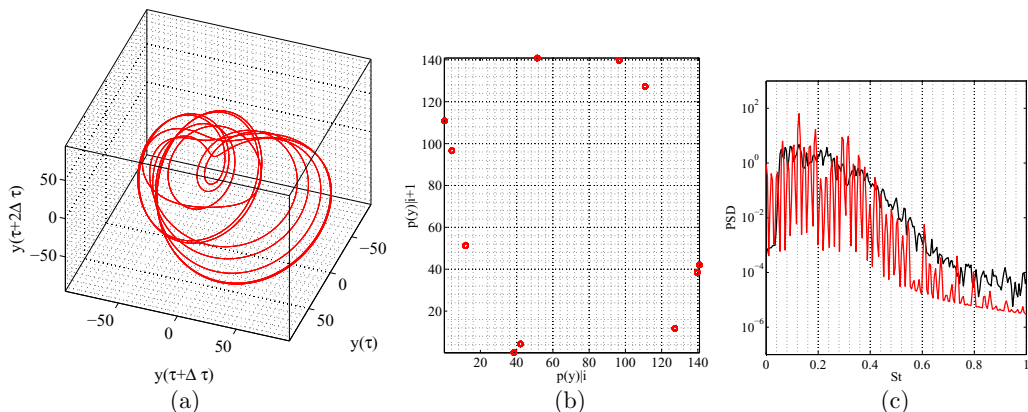


FIG. 16. Asymptotic behavior for N-ARMA model LC shown in Figs. 15(a)–15(e): After the transient, the system settles on a stable limit cycle. In panel (a) the phase space is shown (embedding delay $\Delta t \approx 0.3$); in panel (b) the first-return map is shown [blue dots of Fig. 15(e)].

would evolve after some transient on the surface of a 2-torus (T2) or a limit cycle. In models T-LC, however, one limit cycle (at least) is stable and attracting. Therefore, the hypothetical underlying chaotic toroidal set is only transient, in the sense that the resulting dynamics is due to nonattracting sets in the phase space.

3. Model S

In this section, we analyze a third model, depicted in Fig. 18 and based on a shorter window of correlation. Also in this case, the peak in frequency occurs at $St \approx 0.25$, as shown in the autoregressive PSD analysis in Fig. 18(b); this same dominance is observed in the Welch analysis in Fig. 18(c). The resulting behavior in phase space and in the first return map is rather distinctive and different than the previous models. In particular, this model appears to slowly evolve in time as shown by the first return map; we can conjecture that the model captures some inherent mechanisms associated with wave-packet interactions driven by stochastic turbulence.

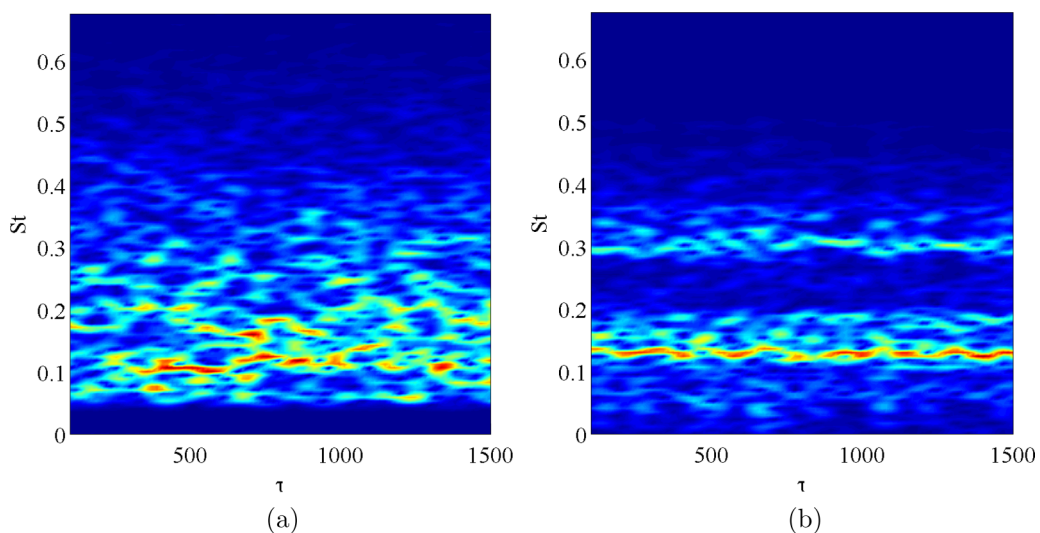


FIG. 17. Spectrogram: Comparison between the original time series and the model LC. (a) TS-POD at $x/D = 5.7$ and (b) Model 2 at $x/D = 5.7$

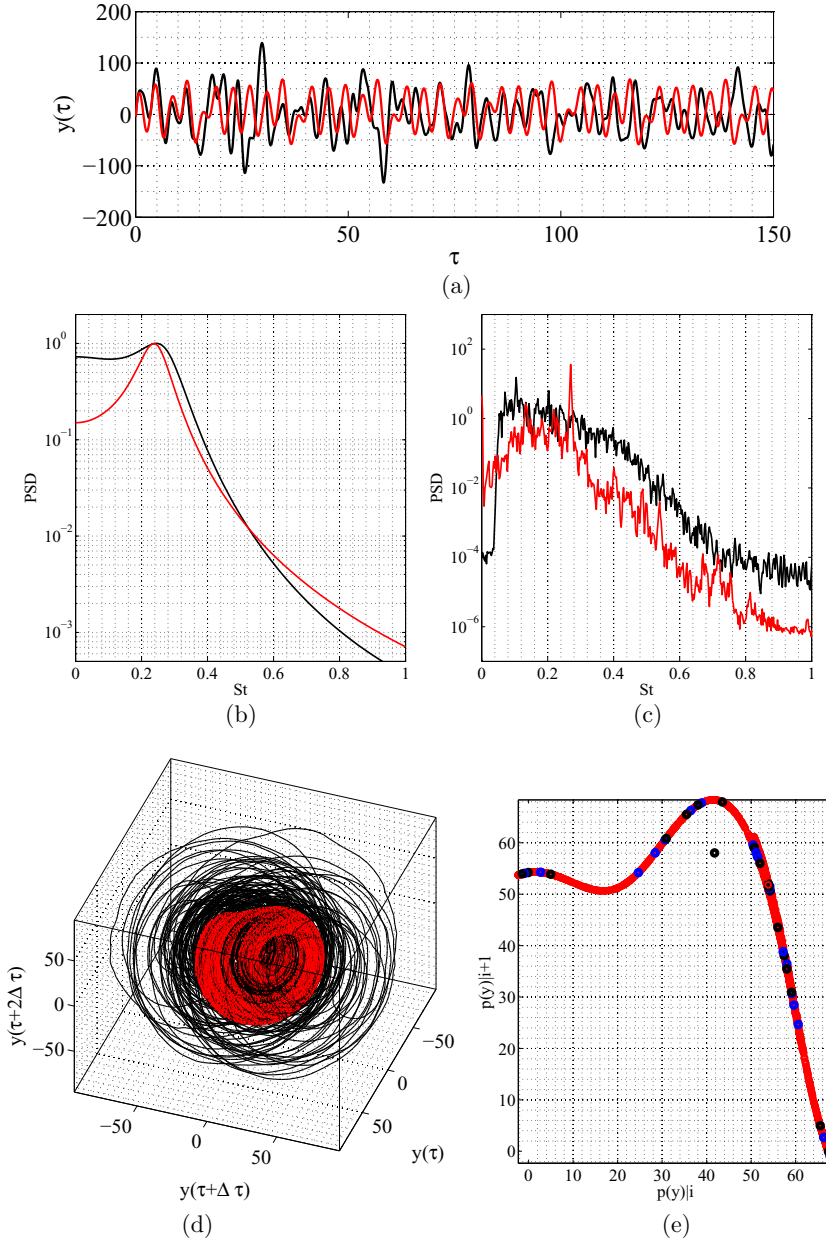


FIG. 18. The comparison between the data obtained from the N-ARMA model S (in red for all the insets) and the original time-series TS-POD at $x/D = 5.7$ (in black) is shown in panel (a). Spectral analysis and phase space reconstruction are shown in panels (b) and (c). The embedding space for the phase space reconstruction (d) is obtained with a delay $\Delta t \approx 0.3$. The first-return map is obtained using the maximum values in the model (e); the black dots correspond to the beginning of the trajectory, while the superimposed blue dots are the last points of the simulation.

D. Discussion: Limits, robustness, and interpretation of the autonomous models

The identified models provide a qualitative, partial, representation of the dynamics. The results need to be discussed and analyzed from both numerical and theoretical points of view. First of all, we

need to stress that for convective systems, analysis on long windows of assimilation is only possible in the presence of an exogenous, known forcing, decorrelated from the outputs, that enhances the identifiability of the system. In Sec. IV B we considered a rather different case, where the inputs were highly correlated with the output; as shown, this allows for the computation of transfer functions, poor from the point of view of educing the internal dynamics but suitable for control design. In principle, one should either consider a decorrelated input or neglect this entirely and cautiously choose short learning windows.

Considering the available dataset, we pursued the second choice, identifying autonomous, output-only polynomial models. In particular, we explored the dynamics of the organized behavior observed in the spectrogram of Fig. 6, trying to separate the endogenous dynamics observable in short windows of observation from the effects of noise sensitivity. We deemed it adequate for analysis of the endogenous dynamics to consider a time length roughly corresponding to the organized events observed in the spectrogram (see Appendix C).

Starting from these choices, we obtain a qualitative picture of the dynamics, which we summarize here. We conjecture that the jittering behavior discussed in the introduction is a mixture of stochastic and deterministic components. Model T and model LC indicate that frequencies can lock together, leading to nonlinear wave-wave interactions. Eventually, in the absence of exogenous stochastic forcing, these could converge on to limit cycles or trajectories embedded on a toroidal surface in phase space. This is also corroborated by the robustness of the models with respect to the initial conditions; i.e., they show the same asymptotic behavior in the presence of uncertainties in the initial conditions. Also, we observed that the present models are rather robust with respect to the position x/D ; the optimization procedure leads to models with different coefficients α , but similar dynamics can be observed from the phenomenological point of view for positions close to the one considered here. Following this rationale, one might imagine the phase space as a dense ensemble of trajectories evolving on limit cycles and toroidal surfaces, associated with wave-wave interactions.

Due to the sensitivity of the system to endogenous forcing, however, the system will continuously and erratically deviate from these attracting solutions without setting on any one of them as observed in the spatiotemporal plots and the spectrogram in Sec. III. This picture is consistent with the high sensitivity to exogenous forcing, typical of the convective flows and can be linked to recent ideas regarding wave-packet theory: the organization observed is understood as being due to the resolvent operator forced by background turbulence. In this sense, the resolvent operator is an *organizer* of the flow, while the turbulence that forces wave packets via this operator is a *disorganizer*. In other words, the jitter signature is deterministic, but it is randomized due to continuous forcing by stochastic background turbulence. The dynamical systems reproduced by model T and model LC evolve according to initial conditions and a dynamic law that cannot evacuate the information convectively, as the jet does. Finally, note that the exogenous term may also include contributions from higher order azimuthal modes $m_\theta > 0$ and their nonlinear interactions, due to our choice of restricting the analysis to the axisymmetric perturbation.

V. CONCLUSIONS AND FINAL REMARKS

Coherent large-scale structures in turbulent jets—wave packets—have been the subject of numerous investigations because of the role they play in sound radiation. It has been established that certain aspects of the wave-packet dynamics can be modeled by means of a linear ansatz [41]. In this work, we consider an unforced, isothermal, subsonic jet issuing from a round nozzle with a fully turbulent boundary layers at $\text{Re} = 5.7 \times 10^5$ and $\text{Ma} = 0.6$. The temporal behavior of the axisymmetric wave packets is analyzed; starting from the studies in Ref. [39], we investigate the experimental, spatiotemporal measurements from a dynamical-systems point of view. The key point is the remarkable spatiotemporal organisation of the measurements despite the high Reynolds number. This observation raises questions regarding the underlying dynamics of the wave packets, the nature of the nonlinearities involved, and the possibility of designing control strategies starting

from this knowledge. With this in mind, a variety of strategies ranging from statistical tools to system identification have been implemented to analyze the data.

Estimation of the correlation and embedding dimensions of the dynamical system confirmed that the organized temporal behavior is low dimensional and deterministic. The minimal embedding ranges from $m = 10$ to $m = 15$, while the correlation dimension is rather low at locations corresponding to the end of the potential core, $d_2 \approx 7$. These dimensions are nonetheless too large for useful characterization of the attractor geometry.

Given the convective character of the flow, system identification is used to compute nonautonomous, input-output models, where the inputs are represented by local measurements taken upstream of the outputs. These models are filters that account for (i) the time delays and (ii) modulation of the amplitudes and frequencies that exist in the inputs. Interestingly, we find that for the convective, input-output modeling nonlinear terms are not necessary: If the inputs already contain a large part of the dynamics, a linear filter is enough to optimally reproduce the temporal behavior at downstream locations. This is an important result as it makes these models particularly well suited for control design based on linear estimators. The lack of robustness is the main limit for these linear filters; however, in our opinion, this might be more of a problem of controllability of the flow, rather than a lack of observability and predictability. By applying strategies such as adaptive control or loop-shaping robust control one might tackle these difficulties, possibly including the effects of the actuation on the real flow during the modeling step.

We have also attempted to characterize the nonlinear dynamics of the time series, considering single-point measurements at different streamwise locations; we replace the original dynamics with surrogate, autonomous, nonlinear models. From the modeling point of view, these surrogate models correspond to an ideal case where only endogenous nonlinear interactions are considered. In that sense, these models can only reproduce a limited part of the dynamics. By comparing the results from three different classes of model, we suggest that the jittering wave-packet dynamics be described in terms of a combination of exogenous and endogenous mechanisms. In this limit, the dynamics of the system would be dominated by wave-wave interactions leading to stable limit cycles and/or solutions lying on toroidal attractors. Evidence for this behavior is provided by the spectral analysis of the transient dynamics of these solutions that qualitatively reproduces the local (in time) dynamics of the original system.

Based on this modeling one can argue that, in the real flow, while the endogenous dynamics are present in the system, wave-wave interactions can never fully take over and the asymptotic behavior of the ideal models can never happen. This interpretation is consistent with the short-lived periods of organized behavior observed in the time-frequency analysis. Short-lived periods of organization cannot be sustained because of the noise-amplifier nature of the jet: Because of the high sensitivity of the system, the trajectory in phase space will continuously escape from these attracting solutions. The organised puffs of Ref. [4] are continuously kicked off their attractors by exogenous forcing by turbulence.

Future work should be devoted to further improving the nonlinear models for the dynamical analysis. While accepting the impossibility of capturing all the features of the system in low-dimensional models, a possible path to improve our understanding of the jittering would be the identification of surrogate models where a stochastic excitation is also included as external forcing. The resulting model would be a nonautonomous one, where the inputs and the outputs are scarcely correlated; in principle, this strategy would help in separating the endogenous mechanisms from the exogenous ones. Moreover, higher order azimuthal modes can be considered, although the interactions among the dominant azimuthal modes within the nonlinear framework would substantially increase the complexity of the problem. Considering the N-ARMAX error equation in Eq. (11), candidate models exploiting the azimuthal interactions would require a polynomial, nonlinear approximation for each of the azimuthal modes and cross terms accounting for the nonlinear interactions. Such a model would result in a rather large optimization problem prone to ill conditioning, due to the presence of null or nearly null entries in the regression matrices. We believe that machine learning techniques may be robust alternatives to classical nonlinear system

identification for properly accounting for the azimuthal interactions among dominant modes and the stochastic forcing. These techniques are quickly spreading in the community as a powerful tool for system identification (see Ref. [63]).

ACKNOWLEDGMENTS

The authors wish to acknowledge Luis A. Aguirre for sharing his system identification package and Christophe Letellier for fruitful discussions. This work is supported by the Agence Nationale de la Recherche (ANR) through the project Cool Jazz (COnTrol-Oriented Linear and nonlinear models for Jet AeroacousticZZ), Grant No. ANR-12-BS09-0024.

APPENDIX A: PRESSURE SIGNAL: PROJECTION ONTO POD MODES

We briefly summarize the postprocessing of the pressure signals. First, a Fourier decomposition is applied such that the series are decomposed into azimuthal modes and frequency components as

$$\tilde{p}_{m_\theta}(x, t) = \tilde{p}(x, m_\theta, t) = \int p'(x, \phi, t) e^{im_\theta \phi} d\phi, \quad (\text{A1})$$

$$P_{m_\theta, \omega}(x) = P(x, m_\theta, \omega) = \int \tilde{p}_{m_\theta}(x, t) e^{-i\omega t} dt, \quad (\text{A2})$$

where ω is the angular frequency. We limit our analysis to the axisymmetric mode, $m_\theta = 0$. The two-point cross spectral matrix (CSM) is formed as

$$\mathbf{R}_{m_\theta, \omega}(x, x_2) = \langle P_{m_\theta, \omega}(x) P_{m_\theta, \omega}^*(x_2) \rangle, \quad (\text{A3})$$

where $*$ indicates the complex conjugate. The Fredholm integral equation on the cone surface (Fig. 2) is given by the relation

$$\frac{2\pi}{\cos \alpha} \int \mathbf{R}_{m_\theta, \omega}(x, x_2, r, r_2) \xi_{m_\theta, \omega}(x, r_2) r_2 dx_2 = \lambda_{m_\theta, \omega} \xi_{m_\theta, \omega}(x, r), \quad (\text{A4})$$

with $r = [(x - X_0) \tan \alpha]$, where X_0 corresponds to the virtual origin of the antenna array and α is the cone half-angle. The eigenvalues and the eigenvectors are given by $\lambda_{m_\theta, \omega}^{(i)}(x)$ and $\xi_{m_\theta, \omega}^{(i)}(x)$, respectively. The kernel $\mathbf{R}_{m_\theta, \omega}(x, x_2, r, r_2)$ is not Hermitian, but it can be made Hermitian by premultiplying it with $\sqrt{rr_2}$; see Ref. [21].

The projection of the complex azimuthal coefficients $P_{m_\theta, \omega}$ onto the basis is performed as

$$b_{m_\theta, \omega}^{(i)} = \int P_{m_\theta, \omega}(x) \xi_{m_\theta, \omega}^{(i)*}(x) dx. \quad (\text{A5})$$

The estimate of the pressure signal in time domain, $\hat{p}_{m_\theta}(x, t)$ is obtained by inverse Fourier transform using the sum

$$\hat{p}_{m_\theta}(x, t) = \frac{1}{2\pi} \int \left[\sum_{i=1}^J b_{m_\theta, \omega}^{(i)} \xi_{m_\theta, \omega}^{(i)}(x) \right] e^{i\omega t} d\omega. \quad (\text{A6})$$

When the number of modes used for the projection equals the number of eigenvectors, $J = N_\lambda$, the estimate $\hat{p}_{m_\theta}(x, t)$ corresponds to the original time series if the computation is performed with the same resolution. Here, different resolutions are adopted for the two campaigns described in Sec. II. In particular, the measurements available from the 4-ring setup provides only a statistical information on a finer, extended grid composed by 22 points. The extrapolation is possible as the first several POD modes on the extended grid are in agreement with the same quantities extracted using the 7-ring setup. For this reason, the data of the coarser mesh of the 7-ring can be properly resampled into the higher resolved 22 points mesh.

APPENDIX B: SYSTEM IDENTIFICATION USING POLYNOMIALS EXPANSION

We have introduced in Sec. IV the basic ideas behind the application of system identification. These tools are used for the qualitative analysis of the observables of the dynamical system and the definition of quantitative control-oriented models. Here, we provide details on the algorithms. We aim at defining polynomial approximation reproducing the temporal behavior of the output $y(t)$. More specifically, we consider the following:

- (1) Nonlinear, autoregressive models reproducing the temporal behavior of the outputs $y(t)$.
- (2) Transfer functions between the inputs $u(t)$ and the outputs $y(t)$.

Here, we discuss the single-input–single-output (SISO) case for sake of conciseness; the extension to the multiinputs-multioutputs (MIMO) cases is rather straightforward from the theoretical point of view. More details can be found in the literature; see Refs. [53–55,58,64].

1. Polynomial models

The equation error model is written using nonlinear Volterra series, based on a polynomial expansion [58]. For instance, at the first order, the polynomial model reads

$$\begin{aligned}
 y(t_n) = & y_0 + \sum_{i=1}^{n_\alpha} \alpha_{(1,i)} y(t_{n-i}) + \sum_{i=1}^{n_\alpha} \sum_{j=1}^{n_\alpha} \alpha_{(2,i,j)} y(t_{n-i}) y(t_{n-j}) + \sum_{i=1}^{n_\beta} \beta_{(1,i)} u(t_{n-i}) \\
 & + \sum_{i=1}^{n_\beta} \sum_{j=1}^{n_\beta} \beta_{(2,i,j)} u(t_{n-i}) u(t_{n-j}) + \sum_{i=1}^{n_\alpha} \sum_{j=1}^{n_\beta} \eta_{(1,i,j)} y(t_{n-i}) u(t_{n-j}) + e(t_n) + O(2), \quad (\text{B1})
 \end{aligned}$$

where α_i , β_i , η_i are the i th-order Volterra coefficients. We can note that the complete model consists of a linear combination of three groups of terms:

- (1) the autoregressive terms, $y(t_n) = f(y(t_n), y(t_{n-1}), \dots, y(t_{n-n_\alpha}))$;
- (2) the exogenous terms, $y(t_n) = f(u(t_n), u(t_{n-1}), \dots, u(t_{n-n_\beta}))$;
- (3) the error $e(t_n)$.

Additionally, the nonlinear combinations are introduced in the full model. The error is computed as a moving average of white-noise process $w(t)$

$$e(t_n) = w(t_n) + \sum_{i=1}^{n_y} \gamma_i w(t_{n-i}). \quad (\text{B2})$$

Both $w(t)$ and the coefficients γ_i are unknowns of the problem.

2. The NARMAX algorithm

The coefficients and the unknown error $w(t)$ can be identified applying the nonlinear autoregressive moving average with exogenous algorithm (NARMAX). Let us consider the sketch in Fig. 19. The identification procedure is based on a regression performed on the available data. Two *time windows* are identified. The number of coefficients n identifies the *window of correlation*: The $(n + 1)$ -th value of the time series is computed as linear combination of the previous n points. All the terms of Eq. (B1) are approximated in this way. The second time length is the *window of assimilation* L : By sliding of a step Δt the window of correlation, it is possible to capture the dynamics of the system by reducing the local bias and averaging over a time horizon indicated by L . Thus, we can form a matrix in Hankel form where L rows of data are gathered; each of the row is composed by n

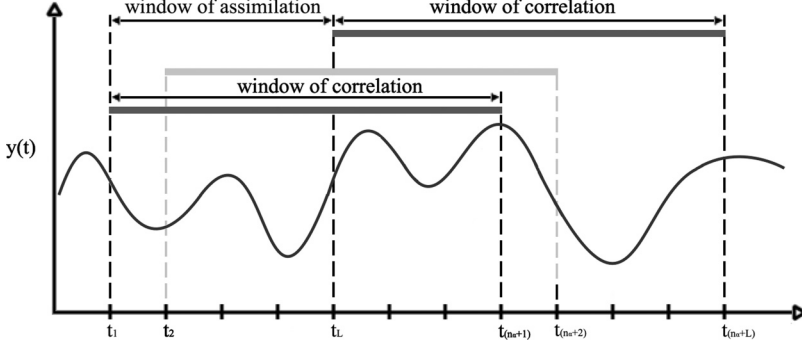


FIG. 19. The sketch exemplifies the identification procedure. The time series $n + 1$ point of the series $y(t)$ is approximated using the previous n entries, included in the correlation window. The assimilation window L is spanned with constant Δt steps, such that the last correlation window covers the entries from $y(t_L)$ to $y(t_{n+L})$.

entries. If we consider the linear SISO case, the following Hankel matrix $\mathbf{H}_N \in \mathbb{R}^{L \times n_L}$ is formed:

$$\mathbf{H}_N = \begin{bmatrix} y(t_1) & y(t_2) & \dots & y(t_{n_\alpha+1}) & u(t_1) & u(t_2) & \dots & u(t_{n_\beta+1}) \\ y(t_2) & y(t_3) & \dots & y(t_{n_\alpha+2}) & u(t_2) & u(t_3) & \dots & u(t_{n_\beta+2}) \\ \vdots & \vdots & & \vdots & \vdots & \vdots & & \vdots \\ y(t_L) & y(t_{L+1}) & \dots & y(t_{n_\alpha+L}) & u(t_L) & u(t_{L+1}) & \dots & u(t_{n_\beta+L}) \end{bmatrix},$$

where both inputs \mathbf{u} and outputs \mathbf{y} are included and $n = n_\alpha + n_\beta$.

The first step of the identification procedure consists of a preliminary computation of the coefficients $\boldsymbol{\theta}^* = [\alpha_1, \alpha_2, \dots, \alpha_n, \beta_1, \beta_2, \dots, \beta_n]$. We assume that the error term $\mathbf{e}(t)$ is null, such that the least-squares regression can be performed as

$$\boldsymbol{\theta}^* = \mathbf{H}_N^\dagger \mathbf{y}. \quad (\text{B3})$$

The preliminary estimation of $\boldsymbol{\theta}^*$ allows the error estimation

$$\mathbf{e}(t) = \mathbf{y} - \mathbf{H}_N \boldsymbol{\theta}^*, \quad (\text{B4})$$

This procedure is prone to inconsistencies; the error $\mathbf{e}(t)$ is modeled as a moving average of white noise $\mathbf{w}(t)$, having expected value $\mathbb{E}[\mathbf{e}(t)] \neq 0$. Due to the expected value of the error $\mathbf{e}(t)$, the estimate of the coefficients $\boldsymbol{\theta}$ will be biased. This limitation is circumvented by introducing a matrix \mathbf{Z}_N of the same dimensions as the Hankel matrix \mathbf{H}_N such that

$$\mathbb{E}[\mathbf{Z}_N \mathbf{y} - \mathbf{Z}_N \mathbf{H}_N \boldsymbol{\theta}^*] = \mathbf{0}. \quad (\text{B5})$$

With a proper choice \mathbf{Z}_N , the debiased estimate of $\boldsymbol{\theta}^*$ is computed as

$$\boldsymbol{\theta}^* = (\mathbf{Z}_N^T \mathbf{H}_N)^{-1} \mathbf{Z}_N^T \mathbf{y}, \quad (\text{B6})$$

if $\mathbf{Z}_N \mathbf{H}_N$ is invertible. This generalization of the least-squares problem is known as instrumental variable (IV). The IV method is iterative. For the first iteration, a rather effective choice for the instruments consists in choosing $\boldsymbol{\eta}(t) = \mathbf{u}(t - n_d)$, i.e., the delayed input. These values are relaxed until convergence (see Refs. [54,55]).

In the presence of nonlinear terms of higher order, nearly null entries of the Hankel matrix can lead to the ill condition of the least-squares process. An iterative orthogonalization can be adopted for preventing the issue. The method, named the orthogonalized least-square (OLS), is adopted in this work [52,58]. The procedure enables us to rank and select only the terms of the original candidate models which are necessary for an optimal representation of the original system.

APPENDIX C: PARAMETERS SPACE OF THE IDENTIFIED MODELS

The NARMAX algorithm described in Appendix B involves numerous choices, leading to a rather large parameter space to be scrutinized. Moreover, due to the nonlinear terms and the complexity of the system, we expect multiple minima for the optimization process. Here, we report and motivate our choices. In particular, we peruse the following parameters: (i) the polynomial order; (ii) the window of assimilation; (iii) the maximum number of coefficients n_α ; and (iv) the optimization parameters. Most of the considerations of this section are done considering the nonlinear models of Sec. IV C. The transfer functions analyzed in Sec. IV B, due to their inherent linearity, result in a much simpler validation analysis.

Polynomial order. We consider as limiting nonlinear order $NL = 3$; the choice is a compromise between numerical and computational issues and the physical description of the system. Preliminary results did not show substantial improvements when introducing higher order nonlinearities in the models. On the other hand, numerical inconsistencies due to singular entries in the Hankel matrices were found when $NL > 3$.

Assimilation window. The spectrogram in Fig. 6 shows that the dynamics is characterized by events at given frequencies corresponding to organized behavior in the time domain. In principle, one should consider more windows of assimilation, stacked over the entire time span, and average the results obtained in these windows of assimilations; however, we consider shorter time windows of assimilation roughly corresponding to the average length of the high-amplitude events observed in the spectrogram. This choice is motivated from the physical point of view by the convective nature of the system, not characterized by specific frequencies of oscillations. We tested windows of length $\tau_{aw} = [20.5, 30.9, 41.2, 61.8, 82.3]$; in the present paper, we consider $\tau_{aw} = 41.2$, which provided best results. The assimilation windows dictate one of the two dimensions of the Hankel matrix.

Coefficients n_α and n_β . The total number of these coefficients dictate the second dimension of the regression matrix, the first being the assimilation window. More importantly, it relates past entries with the actual value $y(t)$ during the autoregression process. We consider the range $n_\alpha = [1, 30]$; the maximum value in convective time corresponds to $\tau \approx 1.25$ and it is based on the analysis of the autocorrelation. Larger values would lead to erroneous correlations between past and present dynamics. The range for n_β is dictated by the convective velocity.

Optimization process parameters. For the optimization process, we consider a maximum of $N_i = 20$ iterations for each model and a maximum of $N_e = 60$ elements for the resulting models, whose 10 terms are related to the error part.

-
- [1] E. Mollö-Christensen and R. Narasimha, Sound emission from jets at high subsonic velocities, *J. Fluid Mech.* **8**, 49 (1960).
 - [2] E. Mollö-Christensen, M. A. Kolpin, and J. R. Martucelli, Experiments on jet flows and jet noise far-field spectra and directivity patterns, *J. Fluid Mech.* **18**, 285 (1964).
 - [3] E. Mollo-Christensen, Jet noise and shear flow instability seen from an experimenter's viewpoint, *J. Appl. Mech.* **34**, 1 (1967).
 - [4] S. C. Crow and F. H. Champagne, Orderly structure in jet turbulence, *J. Fluid Mech.* **48**, 547 (1971).
 - [5] J. C. Lau, M. J. Fisher, and H. V. Fuchs, The intrinsic structure of turbulent jets, *J. Sound Vib.* **22**, 379 (1972).
 - [6] A. Michalke and H. V. Fuchs, On turbulence and noise of an axisymmetric shear flow, *J. Fluid Mech.* **70**, 179 (1975).
 - [7] R. R. Armstrong, A. Michalke, and H. Fuchs, Coherent structures in jet turbulence and noise, *AIAA J.* **15**, 1011 (1977).
 - [8] C. J. Moore, The role of shear-layer instability waves in jet exhaust noise, *J. Fluid Mech.* **80**, 321 (1977).

- [9] A. Michalke, Instability of a compressible circular free jet with consideration of the influence of the jet boundary layer thickness, *Z. Flugwissensch.* **19**, 319 (1971).
- [10] D. Bechert and E. Pfizenmaier, On the amplification of broad band jet noise by a pure tone excitation, *J. Sound Vib.* **43**, 581 (1975).
- [11] J. Cohen and I. Wygnanski, The evolution of instabilities in the axisymmetric jet, part 1: The linear growth of disturbances near the nozzle, *J. Fluid Mech.* **176**, 191 (1987).
- [12] D. G. Crighton and M. Gaster, Stability of slowly diverging jet flow, *J. Fluid Mech.* **77**, 397 (1976).
- [13] P. Plaschko, Helical instabilities of slowly divergent jets, *J. Fluid Mech.* **92**, 209 (1979).
- [14] A. Michalke, A wave model for sound generation in circular jets, Zentralstelle für Luftfahrtokumentation und-information, 1970, <http://elib.dlr.de/63062/>.
- [15] A. Michalke, An expansion scheme for the noise from circular jets, Tech. Rep., DTIC Document, 1971, <http://www.dtic.mil/docs/citations/AD0752169>.
- [16] K. A. Bishop, J. E. Ffowcs-Williams, and W. Smith, On the noise sources of the unsuppressed high-speed jet, *J. Fluid Mech.* **50**, 21 (1971).
- [17] S. C. Crow, Acoustic gain of a turbulent jet, Bulletin of the American Physical Society, paper IE. 6 (1972).
- [18] D. G. Crighton, Basic principles of aerodynamic noise generation, *Prog. Aerospace Sci.* **16**, 31 (1975).
- [19] D. G. Crighton and P. Huerre, Shear-layer pressure fluctuations and superdirective acoustic sources, *J. Fluid Mech.* **220**, 355 (1990).
- [20] T. Suzuki and T. Colonius, Instability waves in a subsonic round jet detected using a near-field phased microphone array, *J. Fluid Mech.* **565**, 197 (2006).
- [21] A. V. G. Cavalieri, D. Rodríguez, P. Jordan, T. Colonius, and Y. Gervais, Wave packets in the velocity field of turbulent jets, *J. Fluid Mech.* **730**, 559 (2013).
- [22] P. Jordan, T. Colonius, G. A. Brès, M. Zhang, A. Towne, and S. Lele, Modeling intermittent wavepackets and their radiated sound in a turbulent jet, in *Proceedings of the Summer Program* (Center for Turbulence Research, Stanford University, 2014), pp. 241–249.
- [23] J. W. Nichols and S. K. Lele, Global modes and transient response of a cold supersonic jet, *J. Fluid Mech.* **669**, 225 (2011).
- [24] X. Garnaud, L. Lesshafft, P. Schmid, and P. Huerre, The preferred mode of incompressible jets: Linear frequency response analysis, *J. Fluid Mech.* **716**, 189 (2013).
- [25] O. Schmidt, A. Towne, T. Colonius, P. Jordan, V. Jaunet, A. V. Cavalieri, and G. A. Brès, Super- and multi-directive acoustic radiation by linear global modes of a turbulent jet, in *Proceedings of the Twenty-second AIAA/CEAS Aeroacoustics Conference* (AIAA, Reston, VA, 2015), p. 2808.
- [26] G. A. Brès, J. Jaunet, M. Le Rallic, P. Jordan, T. Colonius, and S. K. Lele, Large eddy simulation for jet noise: The importance of getting the boundary layer right, in *Proceedings of the Twenty-first AIAA/CEAS Aeroacoustics Conference* (AIAA, Reston, VA, 2015), p. 2535.
- [27] M. Zhang, P. Jordan, G. Lehnasch, A. V. G. Cavalieri, and A. Agarwal, Just enough jitter for jet noise, in *Proceedings of the 20th AIAA/CEAS Aeroacoustics Conference*, AIAA Paper 2014-3061 (AIAA, Reston, VA, 2014).
- [28] Y. B. Baqui, A. Agarwal, A. V. Cavalieri, and S. Sinayoko, A coherence-matched linear source mechanism for subsonic jet noise, *J. Fluid Mech.* **776**, 235 (2015).
- [29] A. V. G. Cavalieri, P. Jordan, A. Agarwal, and Y. Gervais, Jittering wave-packet models for subsonic jet noise, *J. Sound Vib.* **330**, 4474 (2011).
- [30] A. V. G. Cavalieri, G. Daviller, P. Comte, P. Jordan, G. Tadmor, and Y. Gervais, Using large eddy simulation to explore sound-source mechanisms in jets, *J. Sound Vib.* **330**, 4098 (2011).
- [31] F. Kerhervé, P. Jordan, A. V. G. Cavalieri, J. Delville, C. Bogey, and D. Juvé, Educating the source mechanism associated with downstream radiation in subsonic jets, *J. Fluid Mech.* **710**, 606 (2012).
- [32] A. Towne, T. Colonius, P. Jordan, A. V. G. Cavalieri, and G. A. Brès, Stochastic and nonlinear forcing of wave packets in a Mach 0.9 jet, in *Proceedings of the Twenty-first AIAA/CEAS Aeroacoustics Conference* (AIAA, Reston, VA, 2015), p. 2217.
- [33] G. Tissot, M. Zhang, F. C. Lajús, A. V. G. Cavalieri, and P. Jordan, Sensitivity of wavepackets in jets to nonlinear effects: The role of the critical layer, *J. Fluid Mech.* **811**, 95 (2017).

- [34] N. D. Sandham, C. L. Morfey, and Z. W. Hu, Nonlinear mechanisms of sound generation in a perturbed parallel jet flow, *J. Fluid Mech.* **565**, 1 (2006).
- [35] V. Suponitsky, N. D. Sandham, and C. L. Morfey, Linear and nonlinear mechanisms of sound radiation by instability waves in subsonic jets, *J. Fluid Mech.* **658**, 509 (2010).
- [36] K. Sasaki, S. Piantanida, A. V. G. Cavalieri, and P. Jordan, Real-time modeling of wavepackets in turbulent jets, *J. Fluid Mech.* **821**, 458 (2017).
- [37] K. Sasaki, G. Tissot, A. V. G. Cavalieri, S. F. Silvestre, P. Jordan, and D. Biau, Closed-loop control of wavepackets in a free shear flow, in *Proceedings of the 22nd AIAA/CEAS Aeroacoustics Conference*, AIAA Paper 2016–2758 (AIAA, Reston, VA, 2016).
- [38] N. Gautier, J.-L. Aider, T. Duriez, B. Noack, M. Segond, and M. Abel, Closed-loop separation control using machine learning, *J. Fluid Mech.* **770**, 442 (2015).
- [39] D. E. S. Breakey, P. Jordan, A. V. G. Cavalieri, O. Léon, M. Zhang, G. Lehnasch, T. Colonius, and D. Rodríguez, Near-field wave packets and the far-field sound of a subsonic jet, in *Proceedings of the 19th AIAA/CEAS Aeroacoustics Conference*, AIAA Paper 2013–2083 (AIAA, Reston, VA, 2013).
- [40] A. V. G. Cavalieri, P. Jordan, T. Colonius, and Y. Gervais, Axisymmetric superdirectivity in subsonic jets, *J. Fluid Mech.* **704**, 388 (2012).
- [41] P. Jordan and T. Colonius, Wave packets and turbulent jet noise, *Annu. Rev. Fluid Mech.* **45**, 173 (2013).
- [42] F. Takens, Detecting strange attractors in turbulence, in *Dynamical Systems and Turbulence* (Springer, Berlin, 1981), pp. 366–381.
- [43] P. Grassberger and I. Procaccia, Characterization of Strange Attractors, *Phys. Rev. Lett.* **50**, 346 (1983).
- [44] L. Sirovich, Turbulence and the dynamics of coherent structures. I. coherent structures, *Q. Appl. Math.* **45**, 561 (1987).
- [45] S. Narayanan, G. H. Gunaratne, and F. Hussain, A dynamical systems approach to the control of chaotic dynamics in a spatiotemporal jet flow, *Chaos* **23**, 033133 (2013).
- [46] H. Kantz and T. Schreiber, *Nonlinear Time Series Analysis* (Cambridge University Press, Cambridge, UK, 2004), Vol. 7.
- [47] L. Cao, Practical method for determining the minimum embedding dimension of a scalar time series, *Phys. D (Amsterdam, Neth.)* **110**, 43 (1997).
- [48] R. Hegger, H. Kantz, and T. Schreiber, Practical implementation of nonlinear time series methods: The tisean package, *Chaos* **9**, 413 (1999).
- [49] J.-P. Eckmann and D. Ruelle, Fundamental limitations for estimating dimensions and lyapunov exponents in dynamical systems, *Phys. D (Amsterdam, Neth.)* **56**, 185 (1992).
- [50] S. Bagheri, D. S. Henningson, J. Höpfner, and P. J. Schmid, Input-output analysis and control design applied to a linear model of spatially developing flows, *Appl. Mech. Rev.* **62** 020803 (2009).
- [51] D. Sipp and P. J. Schmid, Linear closed-loop control of fluid instabilities and noise-induced perturbations: A review of approaches and tools, *Appl. Mech. Rev.* **68**, 020801 (2016).
- [52] L. A. Aguirre and C. Letellier, Modeling nonlinear dynamics and chaos: A Review, *Math. Prob. Eng.* **2009**, 238960 (2009).
- [53] L. Ljung, in *System Identification: Theory for the User*, Prentice Hall Information and System Science Series, edited by T. Kailath, 2nd ed. (Prentice Hall PTR, Upper Saddle River, NJ, 1999).
- [54] R. Guidorzi, *Multivariable System Identification: From Observations to Models* (Bononia University Press, Bologna, Italy, 2003).
- [55] O. Semeraro and L. Mathelin, An open-source toolbox for linear system identification, Tech. Rep., LIMSI-CNRS, Orsay, France, 2016 (unpublished).
- [56] O. Semeraro, V. Jaunet, P. Jordan, A. V. Cavalieri, and L. Lesshafft, Stochastic and harmonic optimal forcing in subsonic jets, in *Proceedings of the Twenty-second AIAA/CEAS Aeroacoustics Conference* (AIAA, Reston, VA, 2016), p. 2935.
- [57] O. Semeraro, V. Jaunet, A. V. Cavalieri, P. Jordan, and L. Lesshafft, Global resolvent analysis of wave packets in a turbulent jet (unpublished).
- [58] S. A. Billings, *Nonlinear System Identification: NARMAX Methods in the Time, Frequency, and Spatio-temporal Domains* (John Wiley & Sons, New York, 2013).

- [59] N. Fabbiane, O. Semeraro, S. Bagheri, and D. S. Henningson, Adaptive and model-based control theory applied to convectively unstable flows, *Appl. Mech. Rev.* **66**, 060801 (2014).
- [60] O. Semeraro, S. Bagheri, L. Brandt, and D. S. Henningson, Transition delay in a boundary layer flow using active control, *J. Fluid Mech.* **731**, 288 (2013).
- [61] R. Rathnasingham and K. S. Breuer, Active control of turbulent boundary layers, *J. Fluid Mech.* **495**, 209 (2003).
- [62] P. Stoica and R. L. Moses, *Spectral Analysis of Signals* (Pearson Prentice Hall, Upper Saddle River, NJ, 2005), Vol. 452.
- [63] S. L. Brunton, J. L. P. Proctor, and J. N. Kutz, Discovering governing equations from data by sparse identification of nonlinear dynamical systems, *Proc. Nat. Acad. Sci. USA* **113**, 3932 (2016).
- [64] L. Ljung, System identification toolbox for use with MATLAB, Tech. Rep., 2007, https://www.mathworks.com/help/pdf_doc/ident/ident_gs.pdf.